Brookite vs. rutile vs. anatase: What`s behind their various photocatalytic activities?

Gregor Žerjav [a,*], Krunoslav Žižek [b], Janez Zavašnik [c], Albin Pintar [a]

[a] *Laboratory for Environmental Sciences and Engineering, Department of Inorganic Chemistry and Technology, National Institute of Chemistry, Hajdrihova 19, SI-1001 Ljubljana, Slovenia*
[b] *Faculty of Chemical Engineering and Technology, University of Zagreb, Marulićev trg 20, HR-10000 Zagreb, Croatia*
[c] *Centre for Electron Microscopy and Microanalysis, Jožef Stefan Institute, Jamova 39, SI-1000 Ljubljana, Slovenia*

A B S T R A C T

The results of investigating the morphological, optical and electronic properties of three synthesized TiO_2 polymorphs (anatase (A and A2), brookite (B and B2) and rutile (R)) show that the origin of their different catalytic efficiency in the heterogeneous photocatalytic process lies in the depths of the charge carrier traps. The presence of shallow electron traps in brookite extends the number and "lifetime" of generated holes, so brookite is a good choice as a photocatalyst in such heterogeneous photocatalytic systems where these two variables are the reaction limiting factors. Low generation and high recombination rate of charge carriers in rutile are the consequence of too deep electron traps, therefore the generated electrons are not able to participate in reactive oxygen species generation reactions on the catalyst surface. The longer "lifetime" of charge carriers generated in anatase is due to the fact that anatase belongs to the indirect band gap semiconductors. It was further revealed that the increase of the anatase crystallite size (from 10 to 20 nm) can compensate the negative effect of decreasing specific surface area (from 129.5 to 65.0 m^2/g) on the photocatalytic activity of anatase. The negative effect of decreasing specific surface area was very well expressed in the case of brookite, where the photocatalytic activity dropped with decreasing specific surface area (from 17.2 to 3.0 m^2/g) while keeping constant brookite crystallite size ($\approx$ 80 nm). Heterogeneous photocatalytic experiments with the model pollutant bisphenol A show that the deposition of bisphenol A degradation products on the catalyst surface can have a detrimental effect on photocatalytic activity of low specific surface area TiO_2 polymorphs. The specifics (electronic properties, geometry of particles and photocatalytic activity of each TiO_2 polymorph) of the investigated heterogeneous photocatalytic system for reactive oxygen species generation are the reason that the "synergistic effect" between the anatase and rutile phase when used as a physical mixture, regardless of the ratio between them, was not expressed. The anatase phase was shadowed by small and abundant rutile nanoparticles with low photocatalytic activity, which acted also as a harvester of UV-light due to a wider UV-light absorption range. We can conclude that the less studied TiO_2 polymorph brookite is worthy of investigation, as the results of the present study show that the photocatalytic activity of brookite with the adequate specific surface area is comparable to the photocatalytic activity of the widely investigated anatase TiO_2. In addition, it can be concluded that in the physical mixtures of different TiO_2 polymorphs, the use of TiO_2 particles of close diameters is of crucial importance to achieve a "synergistic" photocatalytic effect triggered by particle collisions.

1. Introduction

Titanium dioxide (TiO₂) is one of the most investigated materials used as a catalyst in advanced oxidation processes for various environment applications [1–3]. One of them is heterogeneous photocatalysis for water remediation [4–8], where the catalytic activity of TiO₂ is triggered by light illumination, the energy of which is equal to or higher than the band gap energy of TiO₂. With the illumination of TiO₂, electrons (e^-) are triggered in the valence band (VB) of TiO₂ and injected into the conduction band, leaving a hole (h^+) in the valence band. The generated charge carriers can be further employed to generate reactive oxygen species (ROS), which can be used for the degradation of water

dissolved organic pollutants into CO_2 and water in the final process called mineralization. On the other hand, the generated charge carriers, if not participating in any ROS generation reactions, can recombine and produce energy (i.e. heat). The process of charge carrier recombination has a detrimental effect on the overall photocatalytic activity of a heterogeneous photocatalytic system used for waste water treatment, as the recombined charge carriers are lost for the ROS generation. The main two drawbacks of TiO_2 as a photocatalyst are: (i) its wide band ap of 3.00–3.30 eV (depending on a TiO_2 polymorph used), so the need for UV-light is required to trigger its catalytic activity, and (ii) high charge carrier recombination rate. The three most commonly found TiO_2 polymorphs in nature are: anatase, rutile and brookite [9], of which anatase is the most used and studied for photocatalytic applications, since it mostly expressed higher photocatalytic activity compared to rutile or brookite [10–12]. Rutile is the polymorph with the narrowest band gap of ~3.0 eV, but mostly expresses up to an order of magnitude lower photocatalytic activity than anatase [13]. Di Paola et al. [14] claim that the bottleneck of the use of pure brookite in heterogeneous photocatalysis is the complexity of its synthesis procedure and conclude that its use, although sometimes expressing higher photocatalytic activity than other TiO_2 polymorphs, is not justified. The complex synthesis procedure makes brookite the least studied TiO_2 polymorph. On the other hand, Monai et al. [15] conclude that in-depth studies of brookite, concerning, for example, different band gaps and trap conditions, facial reactivity, crystal structure effect, light reactive oxygen species (ROS) formation, etc., are justified by the fact that its properties are promising for its future use in different applications (photochemical devices, dye-sensitive solar cells (DSSC), biological applications, self-cleaning materials, etc. [16–20]), as it shows better performance than other TiO_2 polymorphs in various photocatalytic reactions (CO_2 photoreduction, ammonia oxidation, oxygen acid photoreforming, etc. [21–24]).

The phenomenon of a synergistic effect between the anatase and rutile phase regarding photocatalytic activity was observed in the past. Mixed phase TiO_2 photocatalyst containing both anatase and rutile expressed higher photocatalytic activity than either pure rutile or anatase phase [25–32]. For example, Degussa TiO_2 powder P-25 is a kind of a standard material in the field of heterogeneous photocatalytic reactions regarding photocatalytic activity, containing rutile and anatase phases in a ratio of about 1:3 [33]. The synergistic effect between the anatase and rutile phase is attributed to the improved separation of UV-light generated charge carriers, although explanations about the mechanism of improved charge separation differ. Some authors claim that the photoexcited electrons (e^-) in rutile migrate to the conduction band of anatase, and the photoexcited holes remain in rutile [26–28]. On the other side, some authors [29,30] observed the opposite direction of electron transfer, namely from anatase to rutile conduction band. We can also find investigations claiming that electrons can migrate in both directions [31], and that holes (h^+) can also migrate from anatase to rutile [32]. Any kind of charge carrier migration between anatase and rutile TiO_2 polymorphs can occur only if there is a contact between the two phases. Most of the authors reported that a close intimate contact between anatase and rutile is required for efficient charge carrier migration/separation, and that only physical mixing of these two TiO_2 polymorphs might not guarantee it [34–37]. However, there are investigations demonstrating that only physical mixing of anatase and rutile could increase the catalytic activity in comparison to pure TiO_2 polymorphs [38–40].

The main aim of the present study was to bring new insights into the understanding of the mechanism of photocatalytic activity of different TiO_2 polymorphs and to better understand differences between them. To achieve this, we synthesized anatase, rutile and brookite TiO_2 polymorphs and evaluate their morphological, optical and electronical properties. Special emphasis was paid to synthesize anatase and brookite polymorphs with different morphological and structural properties and to investigate in-depth how the electronic and optical properties as well

as photocatalytic performance of derived solids depend on them. The synthesis procedures of brookite were designed in a way that the complexity and labor input were in the same range as for anatase. Further, we investigated the ability of synthesized materials to generate ROS under aerobic and anaerobic conditions by using different ROS scavengers. The prepared TiO_2 polymorphs were further used for the degradation of water dissolved bisphenol A (BPA) in the process of heterogeneous photocatalysis. To bring some new understanding into the grey area of photocatalytic activity of mixed TiO_2 phases, especially when physical mixtures of TiO_2 polymorphs are used, ROS generation experiments were conducted with physical mixtures of anatase and rutile and varying ratios between the two phases.

2. Experimental

2.1. Materials

All chemical reagents were used without any purification. The CAS number, source and grade of the chemicals are as follows: titanium dioxide (TiO_2, CristalACTiV™ DT-51, Tronox, ≥99.0%), phosphoric acid (H_3PO_4, 7664–38–2, Merck, ≥85.0%), sodium hydroxide (NaOH, 1310–73–2, Merck, ≥99.0%), titanium isopropoxide (TTIP, 546–68–9, Sigma-Aldrich, ≥97.0%), isopropanol (67–63–0, Merck) and hydrochloric acid (HCl, 7647–01–0, Merck, ≥37.0%).

2.2. Preparation of catalysts

The synthesis of anatase (A) and brookite (B) samples started with TiO_2 nanotubes as a precursor, which were prepared by means of a hydrothermal procedure described in detail in our previous work [41]. 2 g of TiO_2 nanotubes were dispersed in 120 ml of 0.001 M H_3PO_4 and further hydrothermally treated in a Teflon-lined autoclave (24 h, 180 °C). The white product was obtained by centrifugation and then washed several times with ultrapure water (Elga PURELAB Flex, 18 MΩcm) and dried under cryogenic conditions for 24 h (freeze dryer Christ, model ALPHA 1–2 LDplus) to obtain anatase (A). Anatase sample A2 was obtained by calcination of sample A at 550 °C for 24 h.

The synthesis of brookite (B) started by dispersing TiO_2 nanotubes in 200 ml of 0.1 M NaOH. The TiO_2 nanotubes/NaOH solution was hydrothermally treated in a Teflon-lined autoclave for 72 h at 200 °C. Afterwards, was the product obtained by centrifugation and washed several times with ultrapure water and dried for 24 h under cryogenic conditions.

Rutile (R) TiO_2 was prepared using titanium isopropoxide (TTIP, Sigma-Aldrich, ≥97.0%) as a precursor and applying a low-temperature synthesis route proposed by Zhang et al. [42]. TTIP (3.7 ml) was dropwise added to 37 ml of isopropanol under vigorous stirring. After 30 min of stirring, we added dropwise 100 ml of 1 M HCl (the solution was cooled during this procedure on an ice bath). Before leaving the solution for 21 days to stay at room temperature, we stirred it for 4 h. After 21 days, the white precipitate was obtained by centrifugation and washed several times with ultrapure water and dried under cryogenic conditions for 48 h. Afterwards, it was annealed at 450 °C for 3 h.

Brookite B2 was also prepared using TTIP (Sigma-Aldrich, ≥97.0%) as a precursor. In this case, 11.1 ml of TTIP was dropwise added to 50 ml of isopropanol under vigorous stirring. After 30 min of stirring, 200 ml of 0.1 M NaOH was dropwise added to the solution and stirred for another 2 h. Afterwards, the solution was transferred to a Teflon-lined autoclave and heated at 200 °C for 72 h. The material was obtained by centrifugation, thoroughly washed with ultrapure water and dried in an oven at 60 °C for 18 h.

2.3. Characterization methods

N_2 adsorption-desorption isotherms of prepared catalysts were obtained at − 196 °C (Micromeritics TriStar II 3020 analyzer) and used to

determine the specific surface area by means of the Brunauer, Emmett and Teller (BET) theory, total pore volume and average pore size of catalysts. The samples were degassed (Micromeritics SmartPrep degasser) in a stream of N_2 (Linde, purity 6.0) before the analysis following a two-step procedure. During the first step, the samples were degassed at 90 °C for 60 min, which was followed by the second step at 180 °C for 240 min

Field-emission scanning electron microscope (Carl Zeiss, model FE-SEM SUPRA 35 VP) was used to examine the morphology of prepared materials. PANanalytical X`pert PRO MPD diffractometer with Cu Kα1 radiation (1.54056 Å) in reflection geometry (scan range was between 20 and 90° in increments of 0.034°) was used to collect the X-ray powder diffraction (XRD) patterns of the materials. To identify the crystalline phases of measured samples, the obtained XRD patterns were compared to PDF standards from the International Centre for Diffraction Data (ICDD).

The crystal structure and phase composition of such-prepared nanosized particulates were analysed by transmission electron microscope (TEM, JEM-2100, JEOL, Inc.) operating at 200 kV. The micrographs were recorded by slow-scan CCD camera (Orius SC1000, Gatan, Inc.). The powdered samples were first dispersed and sonicated in EtOH(abs) (CAS No. 64–17–5) and transferred by drop-casting onto Ni-supported amorphous lacey carbon grids. A multiple specimen holder (Mod. 667, Gatan, Inc.) was used for sample mounting.

Surface acidic properties were determined with the use of pyridine and a Pyris 1 TGA instrument (Perkin Elmer). To eliminate the surface impurities, the samples were pretreated at 500 °C in air for 15 min. Afterwards, the samples were cooled to 120 °C and purged with pure N_2. Pyridine was then introduced into the N_2 stream until a constant mass was obtained. After that, the samples were purged for 120 min with pure N_2 to completely remove the excess of pyridine before the pyridine time programmed desorption (TPD) measurement. During the pyridine desorption, the samples were heated to 750 °C at a rate of 20 °C/min.

Zetasizer Ultra Red (Malvern Panalytical) was used to determine zeta potential of investigated TiO_2 polymorphs. The system was equipped with an automatic titration device to measure the zeta potential in the pH range from 2 to 9 using NaOH and HCl solutions to control the pH value. Before measurement, the investigated TiO_2 polymorphs (50 mg) were dispersed for 20 min in distilled water (500 ml) using an ultra-flat stirrer (IKA Lab Disc).

Particle size distribution (PSD) of TiO_2 polymorphs A and R was determined in wet mode (samples were previously suspended in demineralized water) by applying the laser diffraction method (Shimadzu, model SALD 3101). Each sample was treated four times under identical process conditions in order to test the reproducibility and to gain more representative size distribution data for each sample. The net size distribution data was provided by *averaging* those 4 size distribution data for each size interval. Averaged PSD is expressed on the basis of volume, with characteristic diameters: d_{50} as a median diameter, d_{mode} as a modus diameter (dominant size in a population), and diameter mean, $d_{3,2}$ and reported via differential distribution function, $dQ_3(d)$. Due to the nanosized particles, the particle size distribution of sample B was measured by multi-angle dynamic light scattering (MADLS, Zetasizer Ultra Red, Malvern Panalytical) using a water suspension containing 240 mg/l of sample B.

The photoresponse characteristics of investigated materials under UV-light illumination (UVA high pressure mercury lamp, 150 W, λ_{max}=365 nm) were evaluated using a Metrohm Autolab PGSTAT30 potentiostat/galvanostat and a three-electrode electrochemical cell. A 0.1 M KOH aqueous solution was used as electrolyte. A screen-printed electrode (DropSens, model DRP-150) presented the working electrode, onto which a 10 µl drop of catalyst-ethanol suspension (12.5 mg of catalyst in 2.5 ml of absolute ethanol (Sigma Aldrich)) was deposited and left to dry. The counter electrode was made of platinum, and the calomel electrode HI5412 (HANNA instruments) presented the reference electrode.

To record UV-Vis diffuse reflectance (DR) spectra of the catalysts, a Perkin Elmer Lambda 35 UV-Vis spectrophotometer, equipped with the RSA-PE-19 M Praying Mantis accessory for powdered samples, was used. White reflectance standard Spectralon© was used for the background correction in the range of 200–700 nm.

A Perkin Elmer UV-Vis fluorescence spectrometer (model LS-55) was used to obtain the photoluminescence (PL) emission spectra of catalysts at the excitation wavelength of 315 nm. To flatten the surface, the catalyst samples were pressed in a holder prior to measurements.

2.4. ROS scavengers

The level of e^- and superoxide anions ($O_2^{\bullet-}$) was measured by the reduction of semi-stable free radical 2,2 ´ -azino-bis(3-ethyl-benzothiazoline-6-sulfonic acid) cation ($ABTS^{\bullet+}$). The latter was prepared by dissolving 17.2 mg of 2,2 ´-azino-bis(3-ethylbenzothiazoline-6-sulfonic acid) salt (ABTS, Sigma) and 3.3 mg of $K_2S_2O_8$ (Aldrich) in 5 ml of distilled water. Before the analysis, the solution was left in the dark at room temperature for 16 h. For the measurements, a reaction suspension containing 1 ml of $ABTS^{\bullet+}$ stock solution, 50 ml of ultrapure water and 5 mg of the catalyst was prepared. The reduction of $ABTS^{\bullet+}$ during UV-light illumination of the catalyst was followed by means of UV-Vis spectrophotometry, as the green color of $ABTS^{\bullet+}$ cation radical solution decolors upon reduction of $ABTS^{\bullet+}$ with e^- or $O_2^{\bullet-}$. Reduction of $ABTS^{\bullet+}$ causes that the intensities of peaks at 345, 395 and 410 nm in the UV-Vis spectra shift.

The level of hydroxyl (OH•) radical formation was measured by using an aqueous solution (50 ml) containing 20 mM NaOH (50 ml, Merck) and 6 mM terephthalic acid (TA, Alfa Aesar, Haverhill, MA, USA). To achieve an adsorption equilibrium before illumination, the suspension containing 10 mg of a catalyst was stirred in the dark for 20 min. During the UVA-light illumination (Prizmatix multichannel LED light source FC2-LED), the aqueous-phase samples were withdrawn in different time intervals and filtered through a 0.2 µm membrane filter. A UV-Vis fluorescence spectrometer (Perkin Elmer, model LS 55) was employed to record the fluorescence signal of the generated 2-hydroxy-terephthalic acid (TAOH) at the excitation wavelength of 315 nm and scanning speed of 600 nm min^{-1} (the widths of the excitation and the emission slits were set to 5 nm). To quantitatively determine the concentration of photogenerated TAOH (or OH•), we used the calibration curve illustrated in Fig. S1, where the PL intensity measured at $\lambda = 425$ nm as a function of TAOH concentration is shown.

2.5. Photocatalytic oxidation experiments

Photocatalytic degradation of bisphenol A (BPA, $c_0 = 10$ mg/l) was conducted in a 250 ml batch slurry reactor (Lenz, model LF60) at constant temperature of 20 °C (Julabo thermostat, model F25/ME) and atmospheric pressure. Bisphenol A (BPA) is an endocrine-disrupting chemical with estrogen-like effects [43], which is widely used by the manufacturers as an intermediate in the production of polycarbonate, epoxy resins and other polymeric materials [44]. Due to its leaching into waste and ground water, BPA presents a potential risk to human health. Concentrations in the range of 0.16–0.36 µg L^{-1} were detected in the wastewater treatment plant effluent in Germany [45]. A maximum concentration of 17.2 mg L^{-1} BPA has been reported in Japanese landfill leachate [46]. The drinking water permissible limit of BPA is 100 µg L^{-1} [47]. During the whole experiment, the BPA solution was purged with purified air (45 l h^{-1}) and stirred at 600 rpm to prevent the sedimentation of catalyst particles (catalyst concentration was 125 mg/l). The suspension was kept in the dark for the first 30 min to establish the sorption process equilibrium, followed by illumination with a UVA high pressure mercury lamp (150 W, $\lambda_{max} = 365$ nm). The UVA lamp was immersed vertically in the center of the reactor in a water-cooled quartz jacket to get an optimal distribution of the light. Degradation of BPA was followed by HPLC analysis (Thermo Scientific HPLC instrument, model

Spectra) with the use of BDS Hypersil C18 2.4 μm column (100 mm × 4.6 mm) and isocratic analytical mode. The column was thermostated at 30 °C, and 70%/30% methanol/ultrapure water solution was used as mobile phase (flow rate was 0.5 ml min⁻¹). The UV detection was performed at $\lambda = 210$ nm. Prior to analysis, the collected aqueous-phase samples (1.5 ml) were filtered through a 0.2 μm membrane filter. The level of mineralization (TOC$_M$) was determined by conducting measurements of total organic carbon (TOC) content in fresh and end-product BPA solution. For this purpose, we used a high-temperature (750 °C) catalytic oxidation (HTCO) method and a TOC analyzer from Teledyne Tekmar (model Torch). The observed error of three repetitions of each analysis was within ± 1%. A CHNS analyzer (Perkin Elmer, model 2400 Series II) was used to determine the amount of accumulated carbon on the catalyst surface during the photocatalytic oxidation of aqueous BPA solution.

3. Results and discussion

3.1. Determination of morphological, optical and electronic properties

The values of measured specific surface area (BET), total pore volume, average pore width, bad gap energies and crystallite size of the prepared materials are summarized in Table 1. The SEM images of prepared TiO$_2$ polymorphs (Fig. 1) show that the morphology of sample A is dominated by small nanoparticles with a BET surface area of 129.5 m^2 g^{-1}. After annealing at 550 °C for 24 h, the specific surface area dropped to 65 m^2 g^{-1}, although the morphology of A2 sample did not change dramatically in comparison to the morphology of sample A. Samples B and R exhibit low but almost the same BET surface areas of 17.2 and 17 m^2 g^{-1} (Table 1). Their morphologies were formed of nanoparticles with length of 100–120 nm and diameter between 50 and 80 nm. The lowest BET surface area of all prepared materials (3 m^2 g^{-1}) was expressed by B2 sample with the "rock" like morphology. The N$_2$ adsorption-desorption isotherms of A, A2 and R samples (Fig. S2) correspond, according to the IUPAC classification, to the type IV isotherms, which are typical for mesoporous materials. Solids B and B2, on the other hand, show typical type II isotherms of nonporous/macroporous materials [48].

XRD diffractograms illustrated in Fig. 2 confirm that the prepared materials consist of only one TiO$_2$ polymorph (anatase JCPDS card no. 71–1167, brookite JCPDS card no. 29–1360 and rutile JCPDS card no. 21–1276). The average crystallite size listed in Table 1 were calculated with the use of the Scherrer equation based on the main diffraction peaks of anatase (101), rutile (110) and brookite (121). The results show the diversity in the average crystallite size of examined TiO$_2$ polymorphs. The highest crystallite size was expressed by brookite samples B and B2 (82 nm), followed by rutile R (21 nm) and anatase A (10 nm). Due to the thermal treatment of sample A at 550 °C for 2 h, growth of anatase crystallites in the A2 sample to 20 nm was observed. This phenomenon was already observed also by Erjavec et al. [49] where a

progressive growth of the anatase crystallites was observed when annealing titanate nanotubes from 300° to 700°C.

The results of the TEM analysis are summarized in Fig. 3. Under the electron beam, the nano-sized samples appear stable, and no alteration during analyses were observed. The phase composition of the samples was probed by selected-area electron diffraction (SAED) method, and match well with the XRD results. The samples are single-phase, corresponding to: samples A and A2 are pure anatase, samples B and B2 are confirmed as brookite, and sample R corresponds to rutile. The ab-initio powder diffraction patterns, used for additional visual confirmation of experimental SAED with simulations, were calculated using the structure data from [50]. No amorphous phases which appear "invisible" for XRD and SAED, were observed on the matching TEM micrographs. The average size of the crystallites is comparable as calculated from XRD data. As observed on HR-TEM micrographs, for anatase sample A (Fig. 3a), the average crystallite size is about 10 nm, while for sample A2 (Fig. 3b) the crystallites are about twice as large, ≈ 20 nm. The crystallites are idiomorphic, with moderately developed morphology: individual facets can be identified in certain orientations, while other surfaces are still not developed well. On the other hand, both brookite samples (Fig. 3c and d) appear to be composed of crystallites of similar size. At first glance, from the low-magnification micrographs (Fig. 3, first column), particles of sample B2 (Fig. 3d) appear much larger than sample B (Fig. 3c), but upon higher magnification we can see that the larger particles of sample B2 are actually agglomerates of semi-textured individual crystallites. When put side-by-side, the individual crystallites are very similar, about 80 nm in size, exhibiting well-developed morphology. The rutile sample (Fig. 3e) is of two types: a bundle of thin needles and cube-like particulates, latter prevailing. Individual needle-like crystals can be as long as 100 nm, while the size of predominant cube-like crystallites is ≈ 20 nm.

The surface acidic properties of prepared materials were evaluated by means of pyridine TPD analysis. The peaks in high- and low-temperature regions in the obtained TPD curves (Fig. 4) can be ascribed to desorption of pyridine from strong and weak acid sites. The TPD curve of solid B shows the presence of three distinguished peaks, while in the TPD curves of A and B2 samples, the presence of two peaks is obvious. Other materials express only one desorption peak. Table 2 summarizes temperatures at which peaks occur, together with the corresponding amounts and densities of acid sites for each investigated solid. The results show that samples with the highest BET specific surface area have the highest number of acid sites, namely 330 and 144 μmol g⁻¹ for A and A2, followed by B (23 μmol g⁻¹), R (20 μmol g⁻¹) and B2 (1 μmol g⁻¹). The linear behavior between the surface area of TiO$_2$ and the surface acidity was also noted by other authors [50].

Fig. 5 presents the results of zeta potential measurements versus the pH value of aqueous suspension for all prepared materials. Minimal but systematic differences between the three investigated TiO$_2$ polymorphs as well as some slight differences between high and low specific surface area anatase and brookite TiO$_2$ polymorphs can be observed. The values of point of zero charge (PZC) of the investigated TiO$_2$ polymorphs decrease in the following order: A (4.45) ≥ R (4.42) ≥ A2 (4.40) >B (4.15) > B2 (4.10). The results show that solids with lower specific surface area tend to result in exhibiting lower PZC values, although the differences in the PZC values under the same TiO$_2$ polymorphs are minimal. These results are in agreement with the observations of other researchers [51,52]. Li et al. [52] concluded that the brookite structure contains the shortest Ti-O bond distance (1.84 Å), which may give rise to sites with the lowest proton affinity among the three TiO$_2$ phases. Correspondingly, the brookite TiO$_2$ polymorphs express the lowest PZC value in comparison to anatase and rutile TiO$_2$ polymorphs. The zeta potential is an important factor which describes the stability of nanoparticles in solutions. If the zeta potential value is above ± 30 mV, maximum aggregation stability is achieved as the particles repel each other and do not undergo flocculation [53,54]. The results in Fig. 5 reveal that for the investigated anatase A and A2 and rutile R TiO$_2$
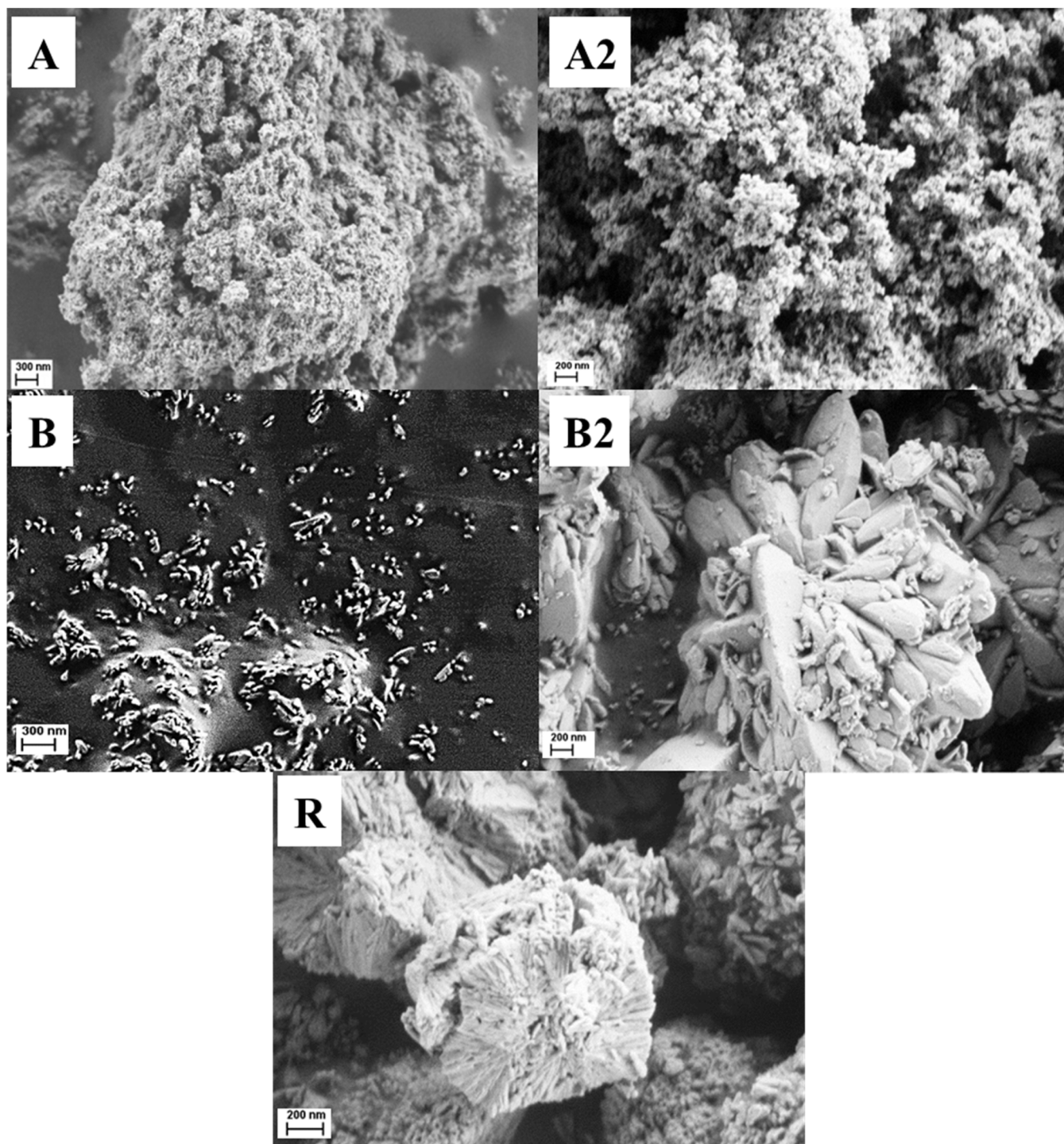
Table 1

Comparison of band gap energy, specific surface area (S$_{BET}$), total pore volume (V$_{pore}$), average pore diameter (d$_{pore}$), and TiO$_2$ crystallite size of studied anatase (A and A2), brookite (B and B2) and rutile (R) samples.

Sample	Band gap, eV	S$_{BET}$ m^2/g	V$_{pore}$ cm^3/g	d$_{pore}$ nm	Crystallite size[a], nm		
					Anatase	Brookite	Rutile
A	3.20	129.5	0.40	10.3	10	/	/
A2	3.15	65.0	0.30	16.0	20	/	/
B	3.30	17.2	0.05	11.6	/	82	/
B2	3.20	3.0	0.01	11.7	/	78	/
R	3.00	17.0	0.05	6.7	/	/	21

[a] The average crystallite sizes were calculated with the use of the XRD diffractograms and the Scherrer equation based on the main diffraction peaks of anatase (101), rutile (110) and brookite (121).

Fig. 1. SEM images of anatase (A and A2), brookite (B and B2) and rutile (R) samples.

polymorphs, two pH regions of the maximum aggregation stability in aqueous suspension occur, namely at pH values below 2.5 and above 6.5. For the brookite samples (B and B2), maximum aggregation stability is available only in the pH region above 5.3. However, heterogeneous photocatalytic experiments with water-dissolved TA and BPA were performed at pH values above 6.5 (pH$_{(TA\ solution)}$ = 12.8), which enabled us high aggregation stability of the suspensions for all investigated samples.

The optical behavior of prepared TiO$_2$ polymorphs was studied by recording UV-Vis DR spectra of catalyst samples (Fig. 6). The obtained band gap energies listed in Table 1 were calculated using the following equation:

$$E_g = \frac{h * C}{\lambda} \qquad (1)$$

where E_g stands for band gap energy (eV), h is the Planck constant (6.626 $\times 10^{-34}$ J s), C is the speed of light (3.0 $\times 10^8$ m s^{-1}) and λ is the cut-off wavelength (nm). The obtained E_g values are 3.2 eV for A, 3.3 eV for B and 3.0 eV for R and are in good agreement with the E_g values of TiO$_2$ polymorphs obtained by other researchers [55,56]. In the case of A2 sample, a slight red shift (3.15 eV) can be observed, which is due to the high annealing temperature of 550 ^{o}C applied during the synthesis
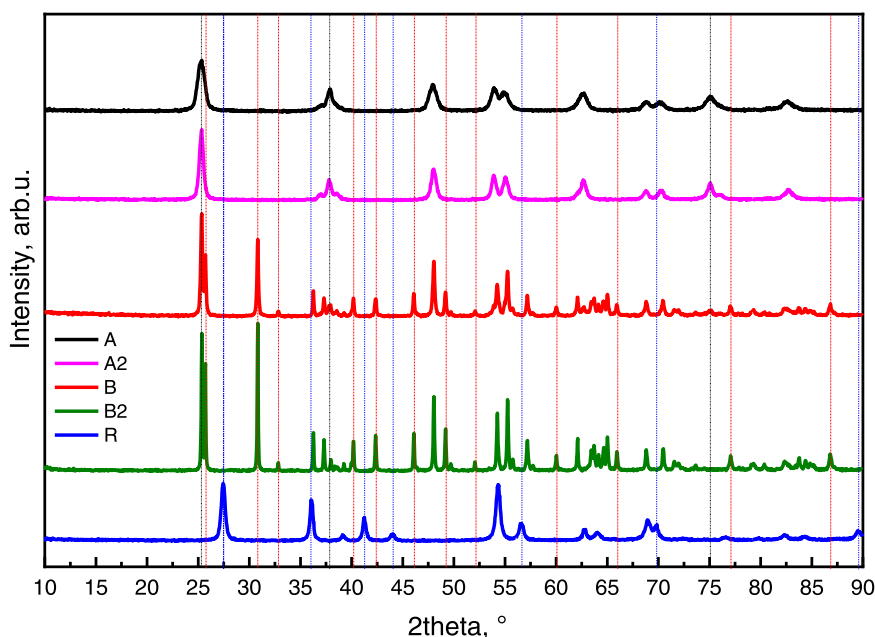
Fig. 2. XRD patterns of anatase (A and A2), brookite (B and B2) and rutile (R) samples. The vertical lines denote the standard data of anatase (black, JCPDS card no. 71–1167), brookite (red, JCPDS card no. 29–1360) and rutile (blue, JCPDS card no. 21–1276).

[57].

One of the main drawbacks of TiO$_2$ as a photocatalyst is high rate of charge carrier recombination, therefore it is of crucial importance to study and understand the fate of light-generated electron-hole pairs. The intensity of the photoluminescence (PL) signal of solids is proportional to the electron-hole recombination rate, as the energy which is released by the recombination of photogenerated electrons (e^-) and holes (h^+) is in the form of PL emissions. The PL spectra of investigated materials are illustrated in Fig. 7. In the PL spectra of A and A2 samples, well-resolved peaks/shoulders at around 3.2, 2.95, 2.8, 2.7, 2.55 and 2.34 eV were observed. Abazović et al. [58] used the calculations from Daude et al. [59] and ascribed the signal in the area of 3.1 eV to direct ($X_{1b} \rightarrow X_{2b}$ at 3.59 eV and $X_{1b} \rightarrow X_{1a}$ at 3.45 eV) and indirect ($X_{1b} \rightarrow \Gamma_3$ at 3.19 eV and $\Gamma_{1b} \rightarrow X_{2b}$ at 3.05 eV) transitions in the anatase TiO$_2$. The well-defined peak at 2.9 eV was ascribed to the lowest indirect transition $\Gamma_{1b} \rightarrow X_{1a}$. The peaks at 2.8, 2.7, 2.55 and 2.34 eV are ascribed to the presence of shallow trap levels. Abazović et al. [59] assigned the high-energy peaks to the band edge luminescence of the anatase TiO$_2$ and the lower-energy peaks/shoulders to the presence of oxygen vacancies. Kernazhitsky et al. [60] ascribed the peaks at 2.71–2.80 eV to the excitonic electron-hole recombination via oxygen vacancies, the strong excitonic peak at 2.91 eV to the recombination of self-trapped excitons and the peaks in the area of 3.0 eV to indirect and direct transitions arising from the band-to-band charge carrier recombination. The presence of oxygen vacancies on the catalyst surface can promote charge transfer and enhance catalyst photocatalytic activity [61]. A comparison of PL spectra of anatase (A and A2) and rutile (R) samples in Fig. 7 reveals a difference between the high-energy bands of anatase and rutile due to differences in the band structure of the two TiO$_2$ polymorphs [59,61]. On the other side, the positions of shallow level traps at 2.8, 2.7, 2.55 and 2.34 eV remained the same. The PL processes in solids are strongly affected by surface and bulk defects, particle size, calcination temperature, etc. [61,62]. Kernazhitsky et al. [61] showed that the increase of specific surface area and associated increase of surface defect states, oxygen vacancies and surface hydration degree result in the enhancement of PL signal in the PL spectra of anatase TiO$_2$. On the other hand, Nakajima et al. [63] reported that the decrease of intensity of PL bands of TiO$_2$ +noble metal composites, in comparison to the intensity of PL bands of pure TiO$_2$ supports, were independent of BET surface area of

materials, so the observed decrease was attributed to differences in the work function between noble metal and TiO$_2$. Liqiang et al. [63] reported that the excitonic PL intensity of TiO$_2$ samples decreased as the calcination temperatures and consequently particle size increased. The PL intensity of sample A2 (Fig. 7) significantly decreased in comparison to the PL intensity of sample A. This can be attributed to the calcination of sample A2 at 500 °C (which means that the amount of surface defects and extent of surface hydration decreased [61]) and growth of anatase crystallite size from 10 to 20 nm. The intensity difference in the PL spectra of brookite samples B and B2 (Fig. 7) can be attributed to the difference in the BET surface area of samples, as synthesis temperature and the brookite crystallite size are the same for both samples. In general, the anatase samples A and A2 expressed the lowest PL intensities and correspondingly the lowest recombination rates of photogenerated charge carriers. This finding is consistent with the results of Zhang et al. [64], who reported that the recombination process of photogenerated charge carriers in TiO$_2$ polymorphs differs due to the fact that anatase is an indirect band gap semiconductor, whereas rutile and brookite are direct band gap semiconductors. This in turn implies that the "lifetime" of photogenerated charge carriers in anatase is longer compared to rutile and brookite.

The ability of the prepared solids for generation and separation of photogenerated electron-hole pairs under UV-light illumination was further investigated by the measurements of current density versus UV-light illumination time (Fig. 8a) and electrochemical impedance spectroscopy (EIS, Nyquist plots in Fig. 9) measurements. Fig. 8a shows that the current density response of examined solids, when UV-light was switched on and off for several cycles, was reproducible for all samples. The highest photocurrent was expressed by the anatase A2 sample, which is not a surprise, as it already expressed the lowest PL intensity among the investigated samples (Fig. 7) and thus the lowest recombination rate of generated charge carriers. The beneficial effect of a large anatase crystallite size on the "lifetime" of photogenerated charge carriers was proved once again, since the photocurrent density of sample A2 was about twice that of sample A. In the case of brookite samples B and B2, higher photocurrent density of sample B is attributed to its higher specific surface area, as brookite crystallite size are the same in both samples. The differences in the responses of photocurrent density rates of TiO$_2$ polymorphs upon switching on and off the UV-light
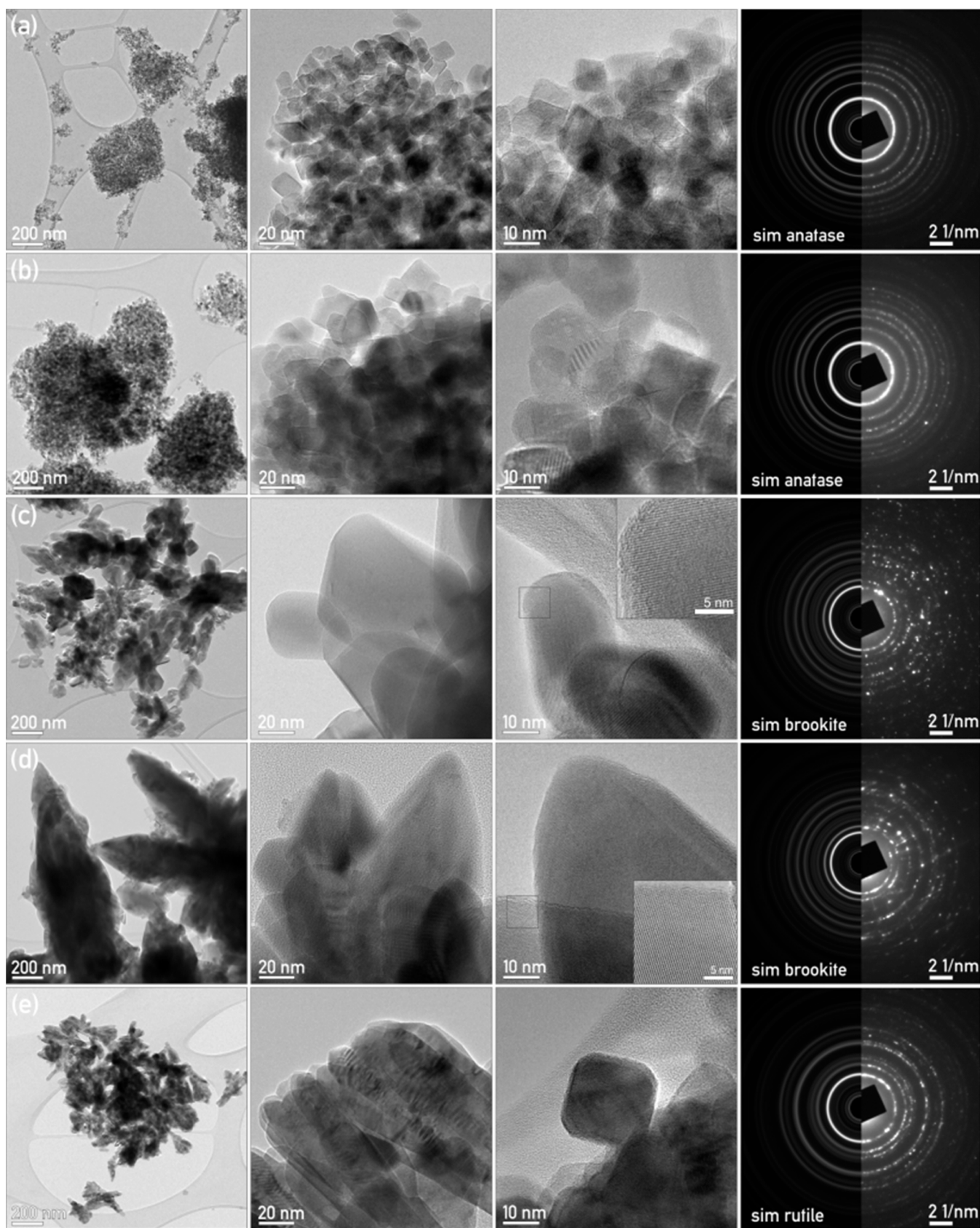
Fig. 3. TEM micrographs of hierarchical investigation of powdered samples; each row corresponds to the following sample: (a) anatase - sample A, (b) anatase - sample A2, followed by (c) brookite - sample B, (d) brookite - sample B2, and (e) rutile - sample R. For direct comparison, each sample in the column was recorded at the same magnification. The images of the last column are composed of experimental SAED pattern (right), and simulated SAED pattern used for phase identification.
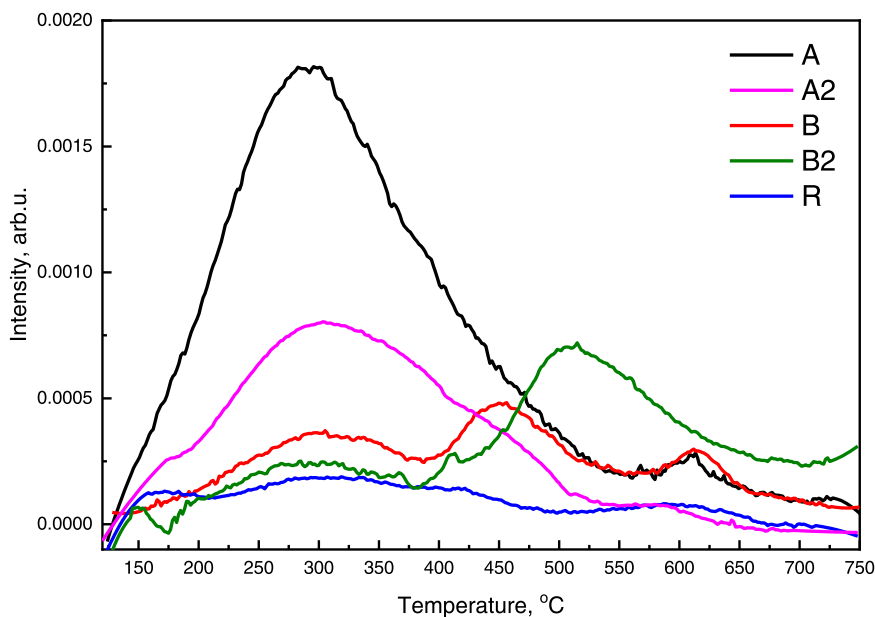
Fig. 4. Pyridine TPD curves of anatase (A and A2), brookite (B and B2) and rutile (R) samples.

Table 2
Density and quantity of acid sites of anatase (A and A2), brookite (B and B2) and rutile (R) samples, corresponding temperatures of pyridine desorption and reaction half-life values ($t_{1/2}$) of BPA degradation.

Sample	Density of acid sites, $\mu mol/m^2$	Amount of acid sites, $\mu mol/g$	Peaks of pyridine desorption,^oC	$t_{1/2}$, min
A	2.5	330	290 (highest), 610	10.8
A2	2.2	144	307	11.3
B	1.4	23	311, 452 (highest), 613	9.3
B2	2.8	1	300, 525 (highest)	77.7
R	1.2	20	/	134.0

illumination are very well expressed in Fig. 7b and c. In the case of anatase and rutile samples, the photocurrent density increases immediately after switching on the UV-light to a constant value (~50 to ~110 s), whereas on the other side, in the case of brookite samples, slow increase of the photocurrent density was observed (~175 s). This can also be attributed to the difference in the mechanism of generating e^- and h^+ under UV-light illumination of TiO$_2$ polymorphs. Vequizo et al. [65, 66] found that the majority of photogenerated e^- in brookite is trapped at defects. This trapping of e^- decreased the number of free e^- but on the other hand extended the "lifetime" and number of h^+ and trapped e^- as the possibility that the trapped e^- and h^+ encounter decreases. This was also well observed in the present study by the slow increase of photocurrent density for brookite samples B and B2 in Fig. 8b after the UV-light was switched on and slow decay of the photocurrent density to zero after the UV illumination was switched off (Fig. 8c). Sopha et al. [67] observed that different TiO$_2$ structures showed different time
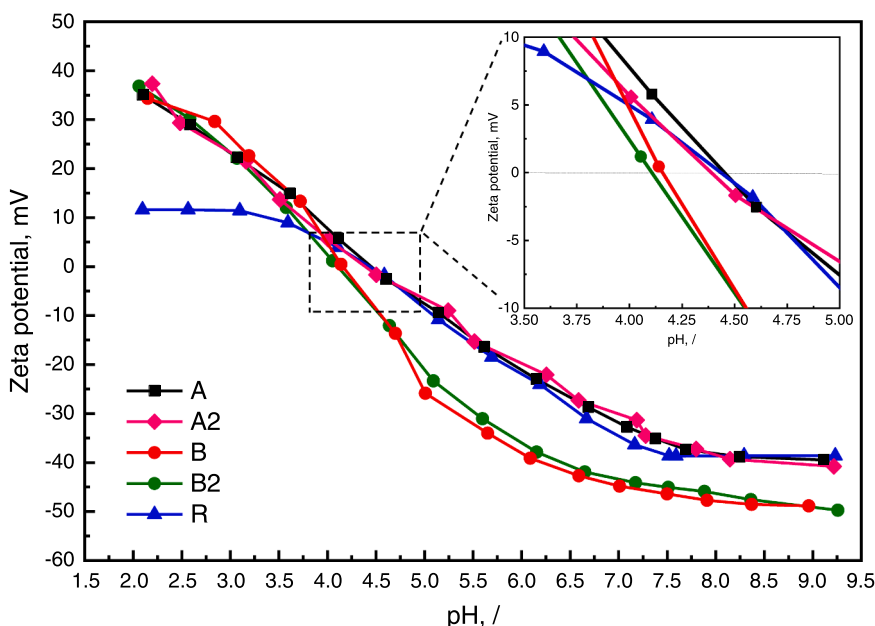

Fig. 5. Zeta potential versus pH value for the investigated TiO$_2$ polymorphs measured in water. The inset shows the point of zero charge (PZC) region.
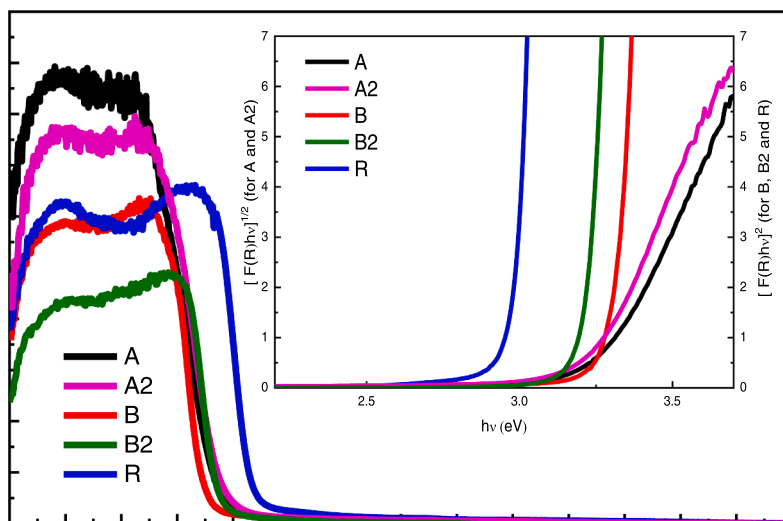
Fig. 6. UV-Vis-DR spectra of anatase (A and A2), brookite (B and B2) and rutile (R) samples. The inset shows the respective Kubelka-Munk function.
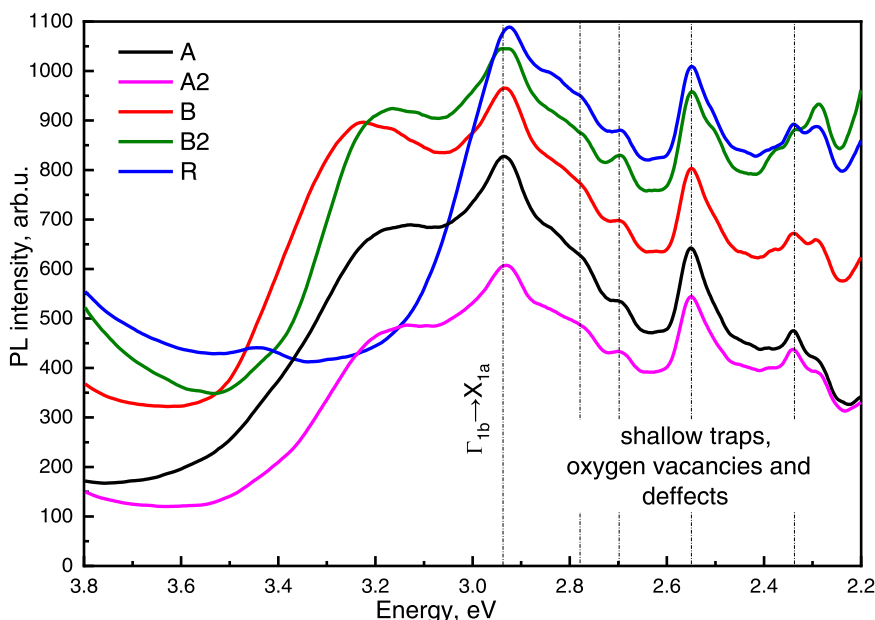

Fig. 7. Solid state photoluminescence (PL) emission spectra of anatase (A and A2), brookite (B and B2) and rutile (R) samples.

intervals required to achieve the maximum photocurrent density after switching the UV-light illumination on. They concluded that the presence of electron traps in TiO_2 results in prolongation of time intervals. Chinonso et al. [68] observed the same phenomenon of slow response of the photocurrent decay to zero after the UV illumination of plasma treated TiO_2-carbon nanotube composite was switched off; they attributed this response to the release of charge carriers from shallow and deep traps. Vequizo et al. [66] report also that in the case of anatase, the e^- trap depth is too shallow to extend the "lifetime" of h^+, whereas in the case of rutile, the depth of e^- trap is too deep, which means that e^- cannot participate in the e^- consuming reactions. Moss et al. [69] discovered that anatase and brookite showed the presence of shallow charge trapping in comparison to rutile, where deeper charge trapping occurred. They concluded that brookite is a good choice as a photocatalyst in reactions where the "lifetime" of charge carriers is the limiting factor. The charge transfer resistance of charge carriers at the surface of examined solids was investigated by EIS measurements; the obtained results are presented in the form of Nyquist plots in Fig. 9. The charge transfer resistance process at the electrode interface and separation of

photogenerated charge carriers are reflected by the diameter of the semicircle in Nyquist plot. A smaller diameter of the semicircle expresses fast charge transfer and efficient separation of electron-hole pairs [70, 71]. The obtained EIS data were well fitted by an equivalent electro circuit presented in Fig. S3, which consists of solution resistance (R_S), charge transfer resistance (R_{CT}), Warburg impedance (W) and constant phase element (CPE). The charge transfer resistance for samples R, B2, A, B and A2 was calculated to be 193, 179, 141, 132 and 48 kΩ, respectively. The obtained charge transfer resistances are inversely proportional to the photocurrent response of the investigated solids illustrated in Fig. 8.

Based on the above, we can summarize that in the case of anatase TiO_2 polymorphs (samples A and A2), larger anatase crystallite size exhibits more beneficial effect on the decrease of charge carrier recombination rate and increased amount of generated charge carriers than high specific surface area. Examination of brookite samples B and B2 shows that at a constant crystallite size, higher specific surface area does beneficially influence the photogeneration of charge carriers. The results of photocurrent measurements suggest that the differences in
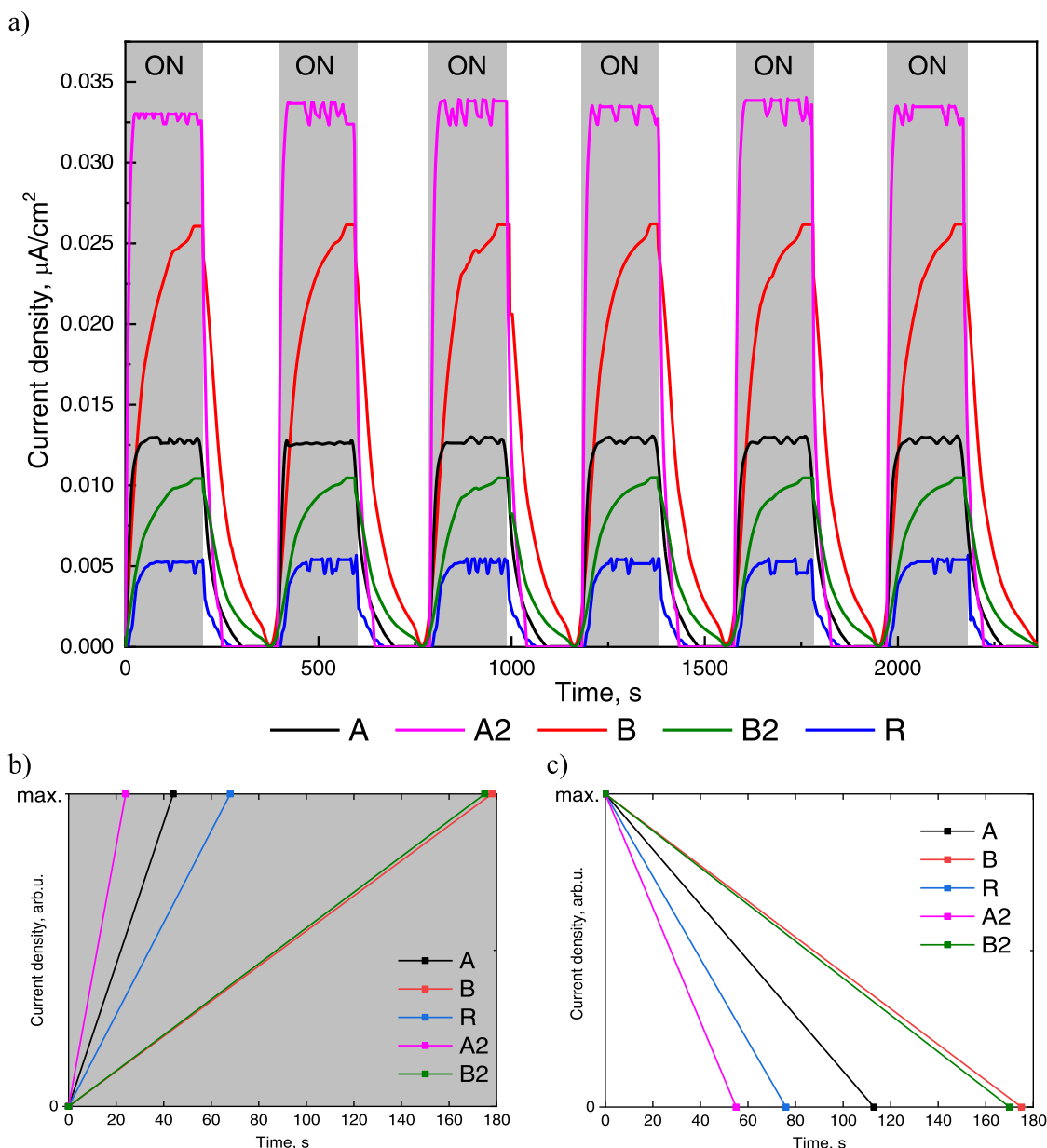
Fig. 8. (a) Off-on current density vs. time traces under UV-light illumination of anatase (A and A2), brookite (B and B2) and rutile (R) working electrode in aqueous solution of 0.1 M KOH. Fig. (b) shows the time needed for each investigated material to reach the constant maximum current density value after switching on the UV-light illumination. Fig. (c) displays the time needed for a decay from the maximum current density to zero after switching off the UV-light illumination.

charge carrier recombination rates of the polymorphs can be attributed to the presence of different depths of e^- traps. High charge carrier recombination rate and low amount of generated charge carriers in the case of rutile sample R can be attributed to too deep e^- traps, which hinders e^- from reaching the catalyst surface.

3.2. Photogeneration of reactive oxygen species and photocatalytic degradation of organic model pollutant bisphenol A

The photogenerated h^+ in the VB of the catalyst are responsible for the mineralization of organic pollutants (Eq. (2)) by (i) direct reaction with the pollutant adsorbed on the catalyst surface or by (ii) reacting with surface adsorbed water (H_2O) and/or hydroxide ion (OH^-) to generate hydroxyl radicals (OH•) (Eqs. (3) and (4)).

$$D_{ads} + h_{VB}^+ \rightarrow D_{ads}^+ \tag{2}$$

$$H_2O + h_{VB}^+ \rightarrow H^+ + \quad OH^\bullet \tag{3}$$

$$OH^- + h_{VB}^+ \rightarrow OH^\bullet \tag{4}$$

To maintain the charge equilibrium and minimize the recombination, e^- in the CB reduce the surface adsorbed oxygen dissolved in water and produce superoxide radical anions ($O_2^{\bullet-}$) (Eq. (5)).

$$O_2 + e_{CB}^- \rightarrow O_2^\bullet \tag{5}$$
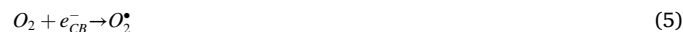
The ability of the prepared solids to produce hydroxyl radicals (OH•) was followed by using terephthalic acid (TA), which upon reaction with the OH·radical forms photoluminescent 2-hydroxyterephthalic acid (TAOH) (Fig. 10). The generation of superoxide radical anions ($O_2^\bullet$) was followed by the reduction of water-dissolved 2,2′-azinobis(3-ethyl-benzothiazoline-6-sulfonic acid) diammonium salt cation ABTS$^{\bullet+}$ [72] (Fig. 11). To study the electronic mechanism a bit further, the reactions in both solutions were performed in the presence and absence of
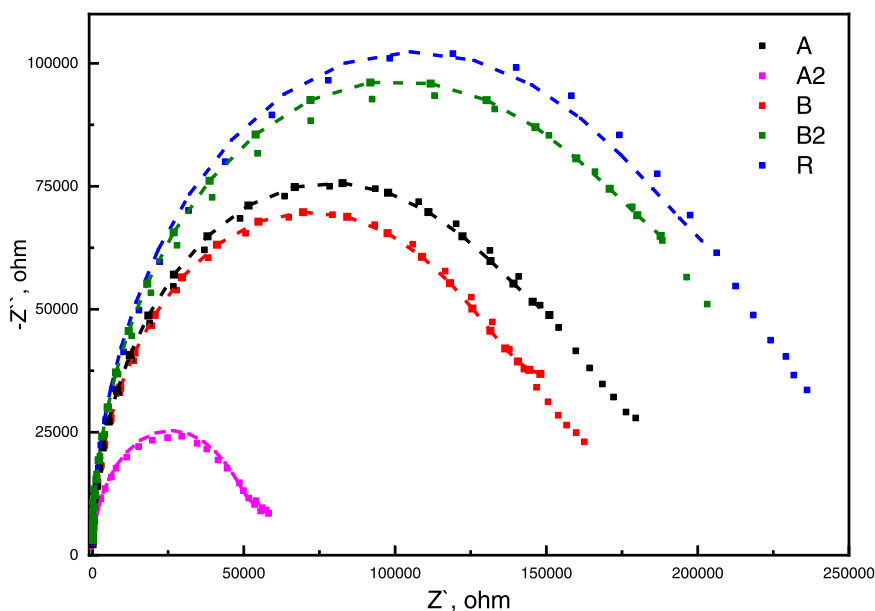
Fig. 9. EIS Nyquist plot of anatase (A and A2), brookite (B and B2) and rutile (R) samples in a 0.1 M KOH electrolyte under UV-light irradiation. The dashed lines are representing the data fitted with the electrochemical equivalent circuit presented in Fig. S3.

water-dissolved oxygen. Water-dissolved oxygen was removed by purging the solutions with pure N_2 (Fig. S4). Regardless of which ROS scavenger was used, the measurements were conducted first for half an hour in the dark to avoid the influence of the scavenger adsorption on the results of ROS photogeneration rates. We can see in Fig. 10 that the highest TAOH generation rate, after 1 h of UV-light illumination, was expressed by the anatase solids A2 (0.8 μM TAOH/h) and A (0.63 μM TAOH/h), followed by brookite sample B (0.54 μM TAOH/h). Solids B2 and R expressed significantly lower TAOH generation rates of 0.058 μM TAOH/h and 0.015 μM TAOH/h, respectively. Sample A2 also expressed the highest rate of ABTS$^{\bullet+}$ reduction (88% after 2 h of UV-light illumination, Fig. 11), followed by sample B2 (67% reduction). The ABTS$^{\bullet+}$ reduction of sample A was significantly lower than that of sample A2 and dropped to 31% after 2 h of UV-light illumination. The lowest ABTS$^{\bullet+}$ reduction rates were expressed by samples R and B2, with 17% and 13%, respectively.

The OH• radical formation rates of all tested solids decreased significantly under anaerobic conditions, indicating that the reaction rate of photogenerated h^+ and surface adsorbed H_2O/OH^- is low. Under anaerobic conditions, the amount of surface adsorbed oxygen is lower, so the e^- are not able to generate $O_2^{\bullet-}$ and maintain the charge equilibrium, because no other electron scavenger was present in the solution. This results in increased charge carrier recombination rates. Czili et al. [73] observed that in the absence of any electron scavenger (dissolved molecular oxygen and/or reducible metal ions), the TiO_2 formation rate of OH• radicals under UV-light illumination was almost negligible. The generated OH• radicals were attributed to some residual oxygen or other impurities in the suspension which expressed electron-acceptor properties. The residual adsorbed oxygen might in our case also be the reason that the solids with the highest specific surface area exhibited noticeable OH• radical formation under anaerobic conditions. This was especially well seen for the anatase samples, where sample A with higher specific surface area generated, under anaerobic conditions, more OH·radicals compared to sample A2. The high catalytic activity of brookite B under anaerobic conditions, although the specific surface area is lower in comparison to anatase samples, can be attributed to the presence of shallow e^- traps, which increase the "lifetime" and number of h^+. The results obtained under anaerobic conditions show that brookite is a good choice for the reactions where the limiting factor is the "lifetime" of charge carriers. The order of the ABTS$^{\bullet+}$ reduction rates of tested solids

was the same under both aerobic and anaerobic conditions. Radical cation ABTS$^{\bullet+}$ can be reduced to ABTS not only via $O_2^{\bullet-}$ (Eq. (5)), but also via the reduction with photogenerated electrons [74]. This means that under anaerobic conditions, ABTS$^{\bullet+}$ acted as an e^- scavenger and thus maintained the charge equilibrium. The lower extent of ABTS$^{\bullet+}$ reduction under anaerobic conditions can be attributed to the fact that the formation of hydroxyl radicals (Eq. (4)) did not occur, so reduction of ABTS$^{\bullet+}$ occurred only through photogenerated e^-.

Further, the photocatalytic activity of prepared TiO_2 polymorphs was tested by using water-dissolved model pollutant bisphenol A (BPA) under UV-light illumination for 60 min. The adsorption equilibrium was determined by keeping the BPA solution in the presence of the TiO_2 polymorphs in the dark for 30 min before the UV-light illumination phase. The results in Fig. 12 show that the adsorption of BPA onto the surfaces of the investigated solids was in the range of 1–2%. The highest BPA degradation rates were measured in the presence of samples B, A and A2, with almost complete BPA degradation after 60 min of UV-light illumination. On the other hand, samples B2 and R converted only 45% and 30% BPA after 60 min of UV-light illumination, respectively (Table S2). The photocatalytic oxidation kinetics of organic pollutants in aqueous solutions is often modeled with the use of the Langmuir-Hinshelwood (L-H) equation (Eq. (6)), which assumes that the reaction takes place on the catalyst surface. In Eq. (6), r presents the reaction rate (mg/(l min)), k the reaction rate constant (1/min), K is the adsorption constant (1/g) and C (mg/l) concentration at time t (min):

$$r = \frac{-dC}{dt} = k * \left(\frac{KC}{1 + KC} \right) \tag{6}$$

Due to the fact that we deal with a low initial concentration (KC is consequently much lower than 1), Eq. (6) can be simplified to a first-order equation (Eq. (7)):

$$r = \frac{-dC}{dt} = k * KC = k' * C \tag{7}$$

where k' presents the apparent first-order reaction rate constant (1/min). The integrated form of Eq. (7) is presented by Eq. (8):

$$C(t) = C_0 * e^{-k' * t} \tag{8}$$

where the initial concentration (mg/l) is presented by C_0. Eq. (8) can be
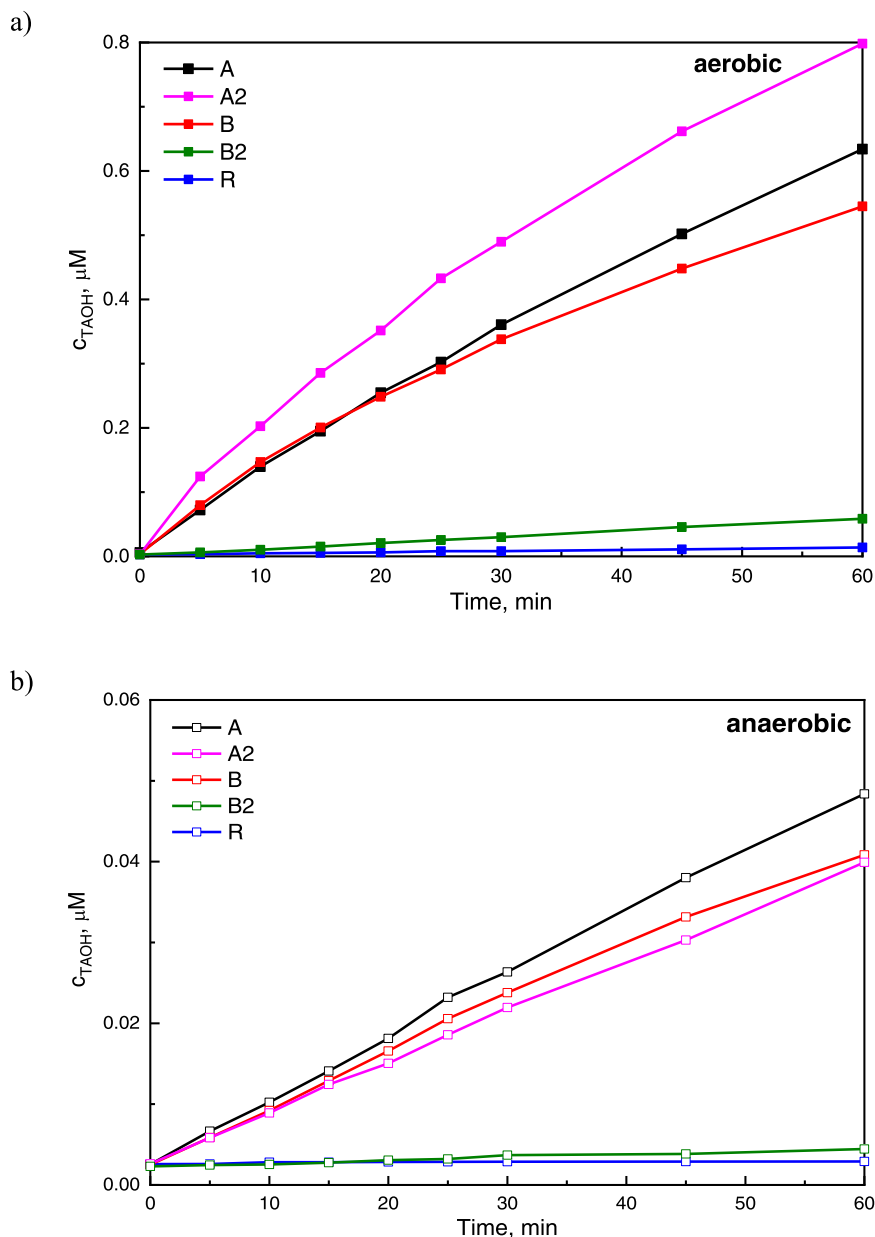
Fig. 10. Concentration of TAOH generated under UV-light illumination of anatase (A and A2), brookite (B and B2) and rutile (R) samples in the presence (a) and absence (b) of oxygen.

linearly expressed (Eq. (9)) by using a logarithmic function:

$$ln\left(\frac{C_0}{C}\right) = -k' * t \tag{9}$$

The slope of the straight line in the plot of $ln\left(\frac{C_0}{C}\right)$ versus time, upon linear regression, equals the apparent first-order reaction rate constant k'. The reaction half-life value ($t_{1/2}$) is the time at which the concentration of the model pollutant is equal to one half of the initial concentration (at t = 0) and is presented by Eq. (10):

$$t_{1/2} = \frac{ln2}{k'} \tag{10}$$

The calculated $t_{1/2}$ values, listed in Table 2, show that morphology, specific surface area and crystallite size of the tested TiO₂ solids influence the photocatalytic BPA degradation rates. The lowest reaction half-life value was expressed by brookite B ($t_{1/2} = 9.3$ min), whereas on the other hand, brookite sample B2 with lower specific surface area

expressed the second highest reaction half-life of 77.7 min. Also, in the case of anatase samples, the reaction half-life of sample A with higher specific surface area is lower ($t_{1/2} = 10.8$ min) than that of sample A2 ($t_{1/2} = 11.3$ min). Considering the results of ROS generation rates and its low specific surface area, it is not surprising that sample R expressed the reaction half-life of 134.0 min. The TOC removal was monitored to obtain data about the mineralization of BPA and reaction intermediates to CO₂ and H₂O, as with HPLC measurements, only temporal BPA concentration was determined (Fig. 12). CHNS analysis of fresh and spent catalysts was performed to obtain data about the adsorption of BPA and/or BPA degradation products onto the catalyst surface. The TOC removal obtained in the presence of examined solids and calculated values of TOC accumulation (TOC$_A$) onto the catalyst surface obtained after 60 min of UV-light irradiation of BPA solution are listed in Table S1. The highest values of mineralization were obtained by anatase A, brookite B and anatase A2, i.e. 94%, 77% and 56%, respectively. For comparison, samples R and B2 exhibited only 14% and 5% of BPA mineralization after 60 min of UV-light illumination. The results of CHNS elemental
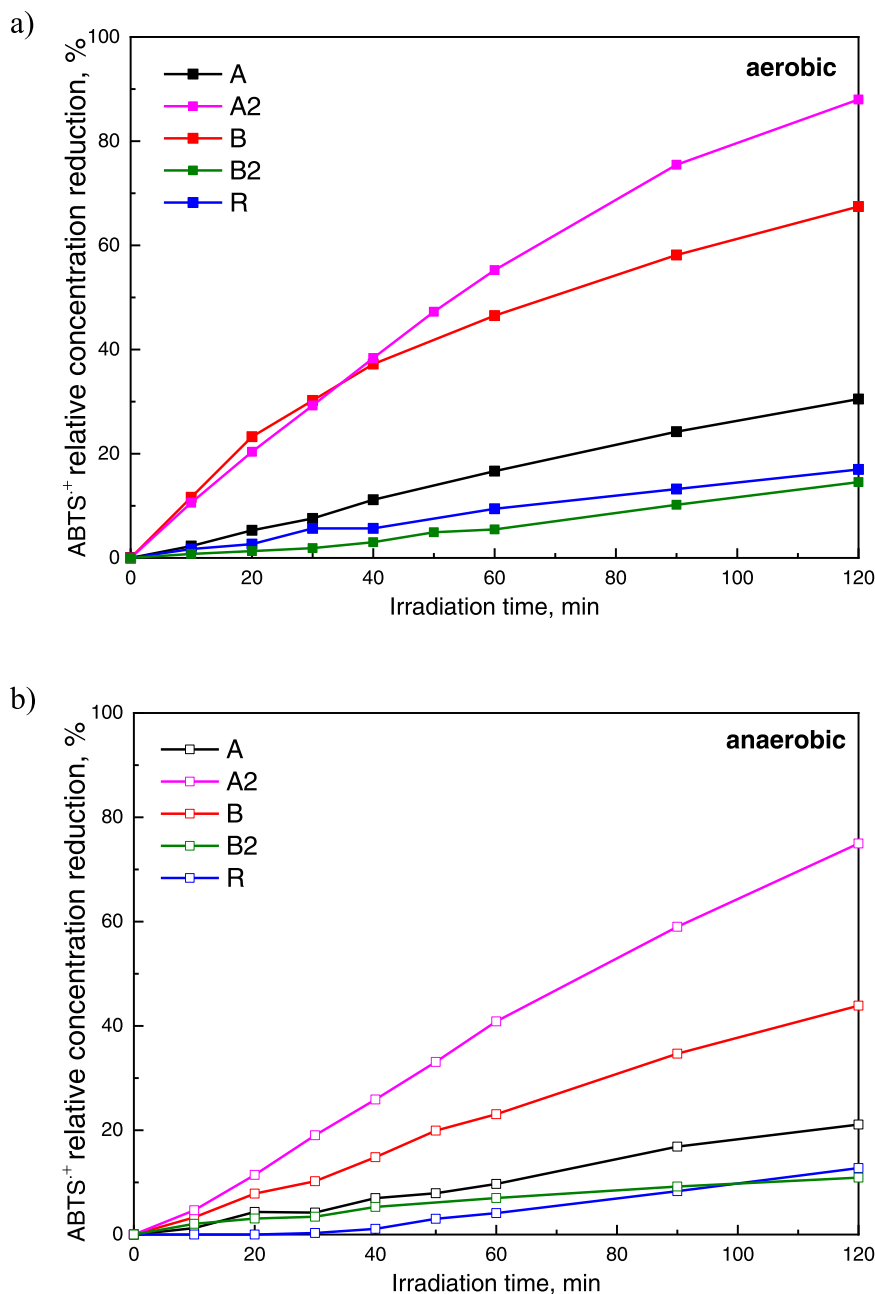
a)

b)

Fig. 11. Dependence of the cation ABTS$^{\bullet+}$ (2,2′-azinobis(3-ethylbenzothiazoline-6-sulfonic acid) diammonium salt) relative concentration on the irradiation time measured upon UV-light exposure of water suspensions of ABTS$^{\bullet+}$ containing anatase (A and A2), brookite (B and B2) and rutile (R) samples in the presence (a) and absence (b) of oxygen.

analysis of anatase and brookite samples show that solids with higher specific surface area tend to accumulate more BPA degradation products onto their surfaces than solids with lower specific surface area, although the solids with higher specific surface area exhibit higher overall mineralization rates. We have to consider that the photocatalytic processes for degradation of organic pollutant in wastewater occur mostly on the catalyst surface. This means that in the case of solids with lower specific surface area, accumulation of even smaller amounts of degradation products on the catalyst surface could detrimentally affect their photocatalytic activity. This was especially well expressed in the case of anatase solids A and A2. Sample A2 exhibited higher ROS generation rates under aerobic conditions (Figs. 8 and 9) than sample A, but in the case of BPA degradation, sample A2 tend to adsorb BPA degradation products (TOC$_A$(A) = 6.2%, TOC$_A$(A2) = 5.7%), which in combination with lower specific surface area resulted in higher reaction half-life

value of sample A2.

3.3. Photogeneration of reactive oxygen species over physical mixtures of anatase A and rutile R TiO$_2$ polymorphs

In addition to runs carried out in the presence of single TiO$_2$ polymorphs, photocatalytic formation of hydroxyl radicals (OH•) under UV-light illumination was also tested in the presence of physical mixtures of anatase (A) and rutile (R) TiO$_2$ polymorphs with different ratios between the two phases (A:R=1:3, A:R=1:1 and A:R=3:1). This was done to investigate if there exists a positive effect on the photocatalytic activity of A:R physical mixtures in comparison to the simulated photocatalytic activities of A:R mixtures, calculated based on activity data obtained from single TiO$_2$ polymorphs.

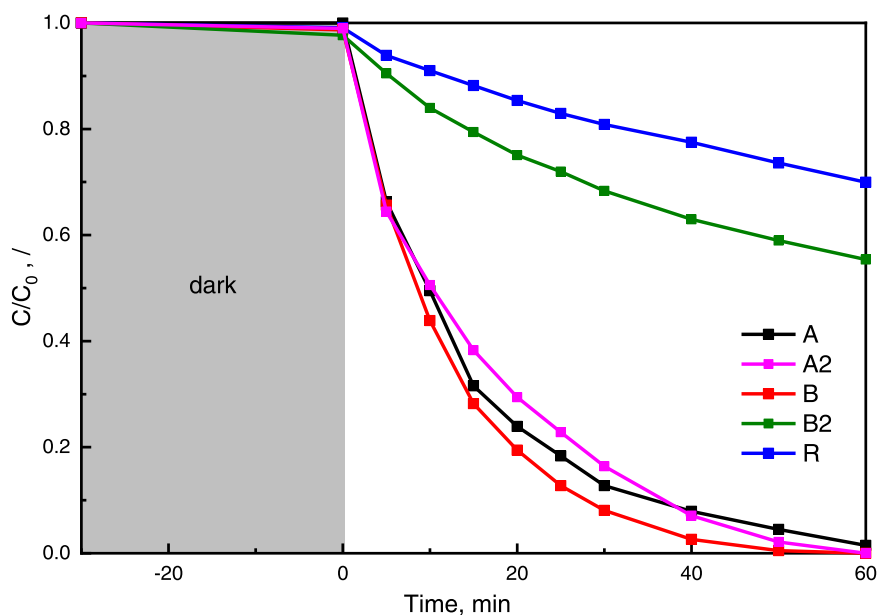The concentration of catalysts in these experiments was kept to

Fig. 12. Photocatalytic degradation of BPA ($c_0 = 10.0$ mg/l) conducted at T = 25 $^{\circ}$C in the presence of anatase (A and A2), brookite (B and B2) and rutile (R) samples under UV-light illumination. Catalyst concentration: 125 mg/l.

10 mg per 50 ml of TA solution. The obtained TAOH generation rates and the simulated generation rates of A:R mixtures, calculated using Eq. (8), are illustrated in Fig. 13. The results show that the actual photocatalytic activities of physical mixtures of A and R are lower than the simulated photocatalytic activities. We can further see in Fig. 13 that the actual amount of generated TAOH after 60 min of UV-light illumination in comparison to the simulated value (if we assume that the simulated amount of generated TAOH is 100%) decreases from 68.8% to 58.2% with the increasing amount of R in the physical mixture. There can be different reasons for this behavior of the physical catalyst mixtures in the investigated heterogeneous photocatalytic system. Some authors claim that the synergistic effect between the A and R phases is dependent on

the irradiation light source used during the photocatalytic tests [75,76]. As can be seen in Fig. S7a, where the UV-Vis DR spectra of A, R and the prepared physical A:R mixtures are presented, the employed anatase A and rutile R have different light-responsive ranges. The band gap energies of pure A and R differ for 0.2 eV, and in the UV-Vis DR spectra of mixtures, we can clearly distinguish between the influences of the two pure TiO_2 phases. The energy spectrum of the UV lamp used is illustrated in the inset of Fig. S7a and shows that the maximum occurs at 360 nm. The results of UV-Vis DR measurements reveal that theoretically in the A:R physical mixtures, the transfer of electrons generated in anatase to rutile (with lower conduction band) would be feasible [40]. With the increasing amount of added R phase, the band gap energy of mixtures
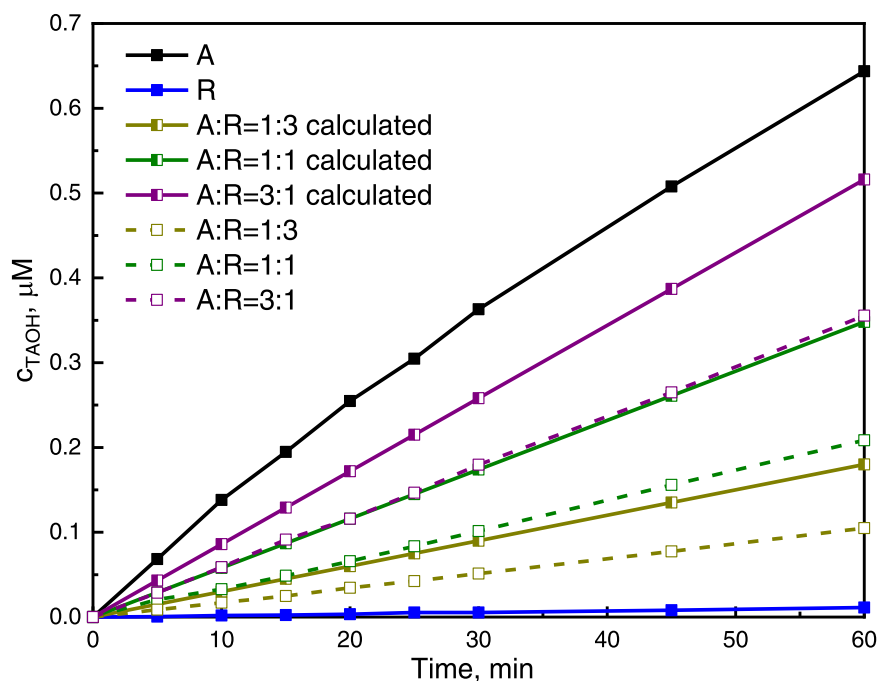

Fig. 13. Concentration of TAOH generated under UV-light illumination of anatase (A) and rutile (R) samples as well as physical mixtures of A+R with different ratios between the TiO_2 phases.

shifts to lower values, which means that the rutile R phase in the mixture would be able to harvest more UV-light than the anatase A phase (Fig. S7a). The ability of rutile TiO$_2$ to absorb UV radiation over a wider wavelength range was observed also by other authors [77]. Further, we measured particle size distribution (PSD) of anatase A and rutile R in wet mode by applying the laser diffraction method (Fig. S8). The measured mean diameter $d_{3,2}$ of anatase A particles was 168.56 and 4.90 μm for the rutile R particles. Considering these values and supposing that the particles have a spherical shape, the external surface area of all anatase A specimens in 10 mg of pure anatase A powder is 1.73 cm^2 (8474 specimens of A) and that of rutile R equals 54.55 cm^2 (257 million specimens of R). The ratio between the external surface area of anatase A and rutile R in the mixtures is presented in Fig. 14. It can be seen that the external surface area of the rutile R part in the mixtures is always higher than the anatase A part, so the rutile R part is always able to harvest more UV-light irradiation than the anatase A part. The effect of the photocatalyst dosage and the so called "shadowing effect" of the catalyst on the efficiency of a heterogeneous photocatalytic system has been widely studied in the past [78–80]. The "shadowing effect" of the separate TiO$_2$ polymorphs was also observed by us in separate tests, where we increased the amount of the photocatalyst during photocatalytic TA oxidation from 5 to 15 mg. Fig. S9 presents the TAOH generation rates of separate TiO$_2$ polymorphs anatase A and rutile R according to the amount of photocatalyst in the reactor system, the simulated TAOH generation rates calculated using Eq. 8 and results of the experiment in which 5 mg of the photocatalyst was introduced into the reactor system. The results in Fig. S9 show that regardless of which TiO$_2$ polymorph was used, the "shadowing effect" took place already when we increased the amount of the TiO$_2$ polymorph from 5 to 10 mg. The amount of generated TAOH with 10 mg loading reached 67.0% (rutile R) and 74.5% (anatase A) of the simulated value. When we increased the loading to 15 mg, the "shadowing effect" was even more pronounced, as the TAOH generation rates in the case of 15 mg of catalyst loading reached only 47.8% (rutile R) and 56.6% (anatase A) of the simulated value. Considering the results of experiments illustrated in Fig. 14 and the results of PSD measurements (Fig. S8), we can conclude that during the TAOH generation experiments with the A:R physical mixtures, the large anatase A particles were "covered" by abundant and small rutile R particles, regardless of the A:R ratio in the mixture, and

that with increasing the rutile R part, the "shadowing effect" of the anatase phase A by rutile R increases. During the execution of photocatalytic TA runs, we could observe that the turbidity of the rutile R/TA aqueous suspension was higher than that of the anatase A/TA aqueous suspension. This might be attributed to the small diameter and better dispersion of rutile R particles in comparison to larger anatase A particles. We also have to point out that in rutile R/TA aqueous suspension, the amount of specimens R is 30,000 × higher than the number of specimens A in the anatase A/TA aqueous suspension. With increased turbidity of the catalyst/TA suspension, penetration of the used UV-light irradiation is hindered and consequently the efficiency of the heterogeneous photocatalytic system.

Kaplan et al. [40] observed a synergistic effect when using a physical mixture composed of anatase and rutile particles for the photocatalytic oxidation of aqueous bisphenol A solution, which is quite similar to the photocatalytic system for TAOH generation investigated in the present study. As reported, higher photocatalytic activity of the physical anatase/rutile mixture originates in the overall increase of hydroxyl radical concentration by the transfer of OH·, generated via H$_2$O oxidation by photogenerated holes in the anatase valence band, from the surface of anatase to rutile during the collision of particles. This means that when the mixture of anatase and rutile is used as the photocatalyst, the anatase part represents the main driving force responsible for the higher overall OH·radical concentration in the system. This was also the fact in our investigated photocatalytic system (Fig. 10), however the anatase part could not generate the same amount of OH·radicals in the mixture as in the case if only anatase would be used, due to the "shadowing" effect caused by small and abundant rutile particles, as discussed above. Further, the rutile particles were acting as a UV-light filter to anatase particles, as they are able to harvest the UV-light illumination in a wider range (Fig. S7a). We can conclude that the "synergistic effect" between the anatase and rutile phase in a physical mixture depends on the specifics of the investigated heterogeneous photocatalytic system, in which besides electronic properties geometry of particles of each TiO$_2$ polymorph and their photocatalytic activity plays an important role.

The same as described above was also observed when physical mixtures composed of anatase A and brookite B and brookite B and rutile R phases were used. In these cases, the "shadowing effect" on photocatalytic TA oxidation was even more pronounced (the results are
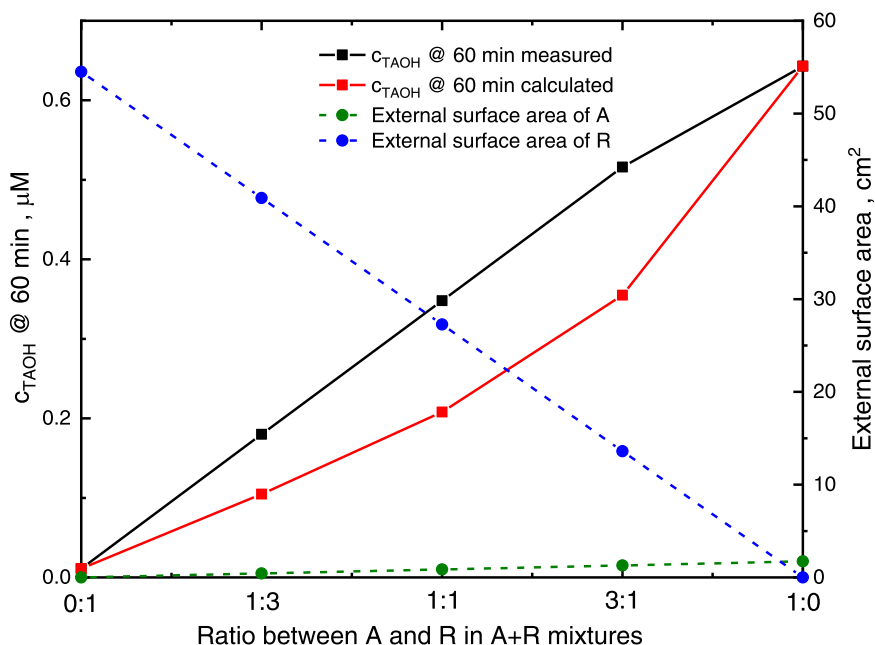

Fig. 14. The amount of generated TAOH after 60 min of UV-light illumination of physical mixtures of anatase A and rutile R in comparison to the simulated values calculated using Eq. (8). Further, the external surface area of anatase A and rutile R phase in dependence of the ratio between A and R in the mixtures are presented.

displayed in Fig. S10), which is due to the use of very small brookite particles with an average particle size of 0.54 μm (Fig. S8c). Assuming that the particles have a spherical shape, this means that the external surface area of brookite B specimens in 10 mg of pure brookite B powder equals 263.11 cm^2 (28,735 million specimens of B). In the physical mixtures of brookite B and rutile R phases, we have to also consider the UV-light filtering effect of rutile R (Fig. S7c) as observed also in the case of the anatase A and rutile R physical mixtures (Fig. S7a). On the contrary, in the physical mixture of anatase A and brookite B, the UV-light filtering effect was absent (Fig. S7b). To obtain a "synergistic" effect exerted by collision of particles of different TiO$_2$ polymorphs, we believe that the particles of each phase should be of a similar diameter.

4. Conclusions

To sum up, three TiO$_2$ polymorphs (anatase (A and A2), brookite (B and B2) and rutile(R)) were synthesized to evaluate the effect of polymorphism and their morphological, optical and electronical properties on the generation of ROS and degradation of bisphenol A in the heterogeneous photocatalytic process. The obtained results suggest that one of the main reasons for different catalytic performance of TiO$_2$ polymorphs is the depth of charge carrier traps. The slow increase and decrease of the photocurrent density of brookite sample after switching the light on and off shows that the photogenerated e^- are trapped at shallow traps, which decreased the number of free e^- but on the other hand extended the "lifetime" and number of h^+. The presence of shallow e^- traps in brookite was further confirmed by the results of ROS generation experiments conducted under anaerobic conditions, where the brookite sample exhibited a moderate activity, although its specific surface area was very low. These results suggest that brookite is a good choice as a photocatalyst in cases where the reaction limiting factor is the "lifetime" and the number of generated h^+. In the case of the rutile sample R, too deeply positioned e^- traps were responsible for the fact that the e^- could not reach the catalyst surface and participate in the e^- consuming reactions, which resulted in the lowest charge carrier generation rate and highest charge carrier recombination rate among all tested materials. The high photocatalytic activity of anatase can be attributed to its high specific surface area and the fact that anatase belongs to an indirect band gap semiconductor, which enables its long "lifetime" of generated charge carriers, which is opposite to rutile and brookite being direct band gap semiconductors. The results further show that the negative influence of decreasing specific surface area of anatase onto the photocatalytic activity can be compensated by increasing the anatase crystallite size. On the other side, high specific surface area of anatase A was beneficial in the ROS experiment conducted under anaerobic conditions, as the residual surface adsorbed oxygen participated in the generation of ROS. Lowering of specific surface area of brookite, by keeping crystallite size constant, exhibited a detrimental effect on its photocatalytic activity. The results of photocatalytic BPA degradation runs and CHNS elemental analysis of fresh and spent catalysts show that the deposition of degradation products onto the catalyst surface significantly decreases the photocatalytic activity. In particular, this was obvious in the case of anatase A2 sample, which exhibited the highest rate of ROS generation, but its photocatalytic activity decreased during the BPA degradation due to the blocking of its surface by BPA degradation products. The results of ROS generation measurements with physical mixtures of anatase and rutile show that there is no "synergistic effect" between the two phases in the given range of reaction and operating conditions. This can be attributed to the shadowing of anatase particles by significantly smaller and more abundant rutile particles, which caused that illumination of the anatase phase being the prevailing phase for the production of OH·radicals was hindered. Another fact is that the rutile phase could act as a UV-light filter due to its lower band gap, which enabled it to harvest UV-light over a wider range compared to anatase. The same behavior was also observed when physical mixtures of brookite B and rutile R or anatase A and brookite B were used.

We can conclude that it is of crucial importance to use particles of close diameters to obtain a "synergistic" effect exerted by collision of particles.

CRediT authorship contribution statement

Gregor Žerjav, Albin Pintar: Conceptualization. **Gregor Žerjav, Janez Zavašnik, Krunoslav Žižek**: Investigation. **Albin Pintar**: Resources. **Gregor Žerjav**: Writing − original draft. **Gregor Žerjav, Albin Pintar, Janez Zavašnik, Krunoslav Žižek**: Writing − review & editing. **Gregor Žerjav, Albin Pintar**: Supervision. **Gregor Žerjav, Albin Pintar**: Project administration. **Albin Pintar**: Funding acquisition.

Declaration of Competing Interest

The authors declare that they have no known competing financial interests or personal relationships that could have appeared to influence the work reported in this paper.

Acknowledgments

Appendix A. Supporting information

Supplementary data associated with this article can be found in the online version at doi:10.1016/j.jece.2022.107722.

References

[1] K. Hashimoto, H. Irie, A. Fujishima, TiO$_2$ photocatalysis: a historical overview and future prospects, Jpn. J. Appl. Phys. 44 (2005) 8269–8285.

[2] H. Tong, S.X. Ouyang, Bi.Y.P. Umezawa, N. Oshikiri, M. Ye, J.H. Nanophotocatalytic, materials: possibilities and challenges, Adv. Mater. 24 (2012) 229–251.

[3] S. Horikoshi, N. Serpone, Can the photocatalyst TiO$_2$ be incorporated into a wastewater treatment method? Background and prospects, Catal. Today 340 (2020) 334–346.

[4] V. Likodimos, A. Chrysi, M. Calamiotou, C. Fernández-Rodríguez, J. Doña-Rodríguez, D.D. Dionysiou, P. Falaras, Microstructure and charge trapping assessment in highly reactive mixed phase TiO$_2$ photocatalysts, Appl. Catal. B 192 (2016) 242–252.

[5] O. Al-Madanat, Y. AlSalka, W. Ramadan, D.W. Bahnemann, TiO$_2$ photocatalysis for the transformation of aromatic water pollutants into fuels, Catalysts 11 (2021) 317.

[6] D. Chen, Y. Cheng, N. Zhou, P. Chen, Y. Wang, K. Li, S. Huo, P. Cheng, P. Peng, R. Zhang, L. Wang, H. Liu, Y. Liu, R. Ruan, Photocatalytic degradation of organic pollutants using TiO$_2$-based photocatalysts: A review, J. Clean. Prod. 268 (2020), 121725.

[7] A. Fujishima, X. Zhang, D.A. Tryk, TiO$_2$ photocatalysis and related surface phenomena, Surf. Sci. Rep. 63 (2008) 515–582.

[8] D.A. Keane, K.G. McGuigan, P.F. Ibanez, M.I. Polo-Lopez, J.A. Byrne, P.S. M. Dunlop, K. O'Shea, D.D. Dionysiou, S.C. Pillai, Solar photocatalysis for water disinfection: materials and reactor design, Catal. Sci. Technol. 4 (2014) 1211–1226.

[9] Q. Tay, X. Liu, Y. Tang, Z. Jiang, T.C. Sum, Z. Chen, Enhanced photocatalytic hydrogen production with synergistic two-phase anatase/brookite TiO$_2$ nanostructures, J. Phys. Chem. C. 117 (2013) 14973–14982.

[10] M. Xu, Y. Gao, E.M. Moreno, M. Kunst, M. Muhler, Y. Wang, H. Idriss, C. Woll, Photocatalytic activity of bulk TiO$_2$ anatase and rutile single crystals using infrared absorption spectroscopy, Phys. Rev. Lett. 106 (2011), 138302.

[11] A.L. Linsebigler, G.Q. Lu, J.T. Yates, Photocatalysis on TiO$_2$ surfaces: principles, mechanisms, and selected results, Chem. Rev. 95 (1995) 735–758.

[12] J.G. Li, T. Ishizaki, X. Sun, Anatase, brookite, and rutile nanocrystals via redox reactions under mild hydrothermal conditions: phase-selective synthesis and physicochemical properties, J. Phys. Chem. C. 11 (2007) 4969–4976.

[13] G. Odling, N. Robertson, Why is anatase a better photocatalyst than rutile? The importance of free hydroxyl radicals, ChemSusChem (2015) 1838–1840.

[14] A. Di Paola, M. Bellardita, L. Palmisano, Brookite, the least known TiO$_2$ photocatalyst, Catalysts 3 (2013) 36–73.

[15] M. Monai, T. Montini, P. Fornasiero, Brookite: nothing new under the sun? Catalysts 7 (2017) 304.

[16] C. Magne, S. Cassaignon, G. Lancel, T. Pauporté, Brookite TiO$_2$ nanoparticle films for dye-sensitized solar cells, ChemPhysChem 12 (2011) 2461–2467.

[17] J. Xu, S. Wu, J. Jin, T. Peng, Preparation of brookite TiO$_2$ nanoparticles with small sizes and the improved photovoltaic performance of brookite-based dye-sensitized solar cells, Nanoscale 8 (2016) 18771–18781.

[18] K. Liu, M. Cao, A. Fujishima, L. Jiang, Bio-inspired titanium dioxide materials with special wettability and their applications, Chem. Rev. 114 (2014) 10044–10094.

[19] T. Shibata, H. Irie, M. Ohmori, A. Nakajima, T. Watanabe, K. Hashimoto, Comparison of photochemical properties of brookite and anatase TiO$_2$ films, Phys. Chem. Chem. Phys. 6 (2004) 1359–1362.

[20] A. Naldoni, T. Montini, F. Malara, M.M. Mróz, A. Beltram, T. Virgili, C.L. Boldrini, M. Marelli, I. Romero-Ocaña, J.J. Delgado, V. Dal Santo, P. Fornasiero, Hot electron collection on brookite nanorods lateral facets for plasmon-enhanced water oxidation, ACS Catal. 7 (2017) 1270–1278.

[21] I. Romero-Ocaña, A. Beltram, J.J. Delgado Jaén, G. Adami, T. Montini, P. Fornasiero, Photocatalytic H$_2$ production by ethanol photodehydrogenation: Effect of anatase/brookite nanocomposites composition, Inorg. Chim. Acta 431 (2015) 197–205.

[22] L. Liu, H. Zhao, J.M. Andino, Y. Li, Photocatalytic CO$_2$ reduction with H$_2$O on TiO$_2$ nanocrystals: comparison of anatase, rutile, and brookite polymorphs and exploration of surface chemistry, ACS Catal. 2 (2012) 1817–1828.

[23] T.A. Kandiel, A. Feldhoff, L. Robben, R. Dillert, D.W. Bahnemann, Tailored titanium dioxide nanomaterials: anatase nanoparticles and brookite nanorods as highly active photocatalysts, Chem. Mater. 232 (2010) 2050–2060.

[24] K. Li, B. Peng, T. Peng, Recent advances in heterogeneous photocatalytic CO$_2$ conversion to solar fuels, ACS Catal. 6 (2016) 7485–7527.

[25] T. Ohno, K. Tokieda, S. Higashida, M. Matsumura, Synergism between rutile and anatase TiO$_2$ particles in photocatalytic oxidation of naphthalene, Appl. Catal. A 244 (2003) 383–391.

[26] R. Amal, Y.K. Kho, A. Iwase, W.Y. Teoh, L. Madler, A. Kudo, Photocatalytic H$_2$ evolution over TiO$_2$ nanoparticles. the synergistic effect of anatase and rutile, J. Phys. Chem. C. 114 (2010) 2821–2829.

[27] G.H. Li, C.P. Richter, R.L. Milot, L. Cai, C.A. Schmuttenmaer, R.H. Crabtree, G. W. Brudvig, V.S. Batista, Synergistic effect between anatase and rutile TiO$_2$ nanoparticles in dye-sensitized solar cells, Dalton Trans. (2009) 10078–10085.

[28] G.H. Li, S. Ciston, Z.V. Saponjic, L. Chen, N.M. Dimitrijevic, T. Rajh, K.A. Gray, Synthesizing mixed-phase TiO$_2$ nanocomposites using a hydrothermal method for photo-oxidation and photoreduction applications, J. Catal. 253 (2008) 105–110.

[29] T. Kawahara, T. Ozawa, M. Iwasaki, H. Tada, S. Ito, Photocatalytic activity of rutile-anatase coupled TiO$_2$ particles prepared by a dissolution-reprecipitation method, J. Colloid Interface Sci. 267 (2003) 377–381.

[30] D. Jiang, S. Zhang, H. Zhao, Photocatalytic Degradation Characteristics of Different Organic Compounds at TiO2 Nanoporous Film Electrodes with Mixed Anatase/ Rutile Phases, Environ. Sci. Technol. 41 (2007) 303–308.

[31] Y. Mi, Y. Weng, Band alignment and controllable electron migration between rutile and anatase TiO$_2$, Sci. Rep. 5 (2015) 11482.

[32] A. Kafizas, X. Wang, S.R. Pendlebury, P. Barnes, M. Ling, C. Sotelo-Vazquez, R. Quesada-Cabrera, C. Li, I.P. Parkin, J.R. Durrantt, Where do photogenerated holes go in anatase:rutile TiO$_2$? A transient absorption spectroscopy study of charge transfer and lifetime, J. Phys. Chem. A 120 (2016) 715–723.

[33] B. Ohtani, O.O. Prieto-Mahaney, D. Li, R.J. Abe, What is Degussa (Evonik) P25? Crystalline composition analysis, reconstruction from isolated pure particles and photocatalytic activity test, Photochem. Photobiol. A 216 (2010) 179–182.

[34] G. Li, K.A. Gray, The solid-solid interface: Explaining the high and unique photocatalytic reactivity of TiO$_2$-based nanocomposite materials, Chem. Phys. 339 (2007) 173–187.

[35] P. Apopei, C. Catrinescu, C. Teodosiu, S. Royer, Mixed-phase TiO$_2$ photocatalysts: crystalline phase isolation and reconstruction, characterization and photocatalytic activity in the oxidation of 4-chlorophenol from aqueous effluents, Appl. Catal. B. 160–161 (2014) 374–382.

[36] S.-H. Lin, C.-H. Chiou, C.-K. Chang, R.-S. Juang, Photocatalytic degradation of phenol on different phases of TiO$_2$ particles in aqueous suspensions under UV irradiation, J. Environ. Manag. 92 (2011) 3098–3104.

[37] B. Sun, P.G. Smirniotis, Interaction of anatase and rutile TiO$_2$ particles in aqueous photooxidation, Catal. Today 88 (2003) 49–59.

[38] T. Ohno, K. Sarukawa, K. Tokieda, M. Matsumura, Morphology of a TiO$_2$ photocatalyst (Degussa, P-25) consisting of anatase and rutile crystalline phases, J. Catal. 203 (2001) 82–86.

[39] R. Su, R. Bechstein, L. So, R.T. Vang, M. Sillassen, B. Esbjornsson, A. Palmqvist, F. Besenbacher, How the anatase-to-rutile ratio influences the photoreactivity of TiO$_2$, J. Phys. Chem. C. 115 (2011) 24287–24292.

[40] R. Kaplan, B. Erjavec, A. Pintar, Enhanced photocatalytic activity of single-phase, nanocomposite and physically mixed TiO$_2$ polymorphs, Appl. Catal. A 489 (2015) 51–60.

[41] B. Erjavec, R. Kaplan, P. Djinović, A. Pintar, Catalytic wet air oxidation of bisphenol A model solution in a trickle-bed reactor over titanate nanotube-based catalysts, Appl. Catal. B 132–133 (2013) 342–352.

[42] S. Zhang, C.Y. Liu, Y. Liu, Z.Y. Zhang, L.Y. Mao, Room temperature synthesis of nearly monodisperse rodlike rutile TiO$_2$ nanocrystals, Mater. Lett. 63 (2009) 127–129.

[43] T.J. Woodruff, Bridging epidemiology and model organisms to increase understanding of endocrine disrupting chemicals and human health effects, J. Steroid Biochem. Mol. Biol. 127 (2011) 108–117.

[44] C.A. Staples, P.B. Dom, G.M. Klecka, S.T. O'Blook, L.R. Harris, A review of the environmental fate, effects, and exposures of bisphenol A, Chemosphere 36 (1998) 2149–2173.

[45] W. Korner, U. Bolz, W. Submuth, G. Hiller, W. Shuller, V. Hanf, H. Hagenmaier, Input/output balance of estrogenic active compounds in major municipal sewage plant in Germany, Chemosphere 20 (2000) 1131–1143.

[46] B. Seyhi, P. Drogui, G. Buelna, J.F. Blais, Removal of bisphenol-A from spiked synthetic effluents using an immersed membrane activated sludge process, Sep. Purif. Technol. 87 (2012) 101–109.

[47] K.K. Selvaraj, G. Shanmugam, S. Sampath, D.G.J. Larsson, B.R. Ramaswamy, GC-MS determination of bisphenol A and alkylphenol ethoxylates in river water from India and their ecotoxicological risk assessment, Ecotoxicol. Environ. Saf. 99 (2014) 13–20.

[48] S. Lowell, J.E. Shields, M.A. Thomas, M. Thommes, Corr. 2nd printing, 2004, XIV, ed.. Characterization of Porous Solids and Powders: Surface Area, Pore Size and Density, 1st ed. 2004,,, Kluwer Academic Publishers,, 2004.

[49] B. Erjavec, R. Kaplan, A. Pintar, Effects of heat and peroxide treatment on photocatalytic activity of titanate nanotubes, Catal. Today 241 (2015) 15–24.

[50] J. Papp, S. Soled, K. Dwight, A. Wold, Surface acidity and photocatalytic activity of TiO$_2$, WO$_3$/TiO$_2$, and MoO$_3$/TiO$_2$ photocatalysts, Chem. Mater. 6 (1994) 496–500.

[51] H. Li, M. Vrinat, G. Berhault, D. Li, H. Nie, P. Afanasiev, Hydrothermal synthesis and acidity characterization of TiO$_2$ polymorphs, Mater. Res. Bull. 48 (2013) 3374–3382.

[52] P. Afanasiev, Transfer of stored electrons between TiO$_2$ polymorphs during photocatalytic H$_2$ production in methanol-water medium, Appl. Catal. A 598 (2020), 117548.

[53] I.S. Grover, S. Singh, B. Pal, The preparation, surface structure, zeta potential, surface charge density and photocatalytic activity of TiO$_2$ nanostructures of different shapes, Appl. Surf. Sci. 280 (2013) 366–372.

[54] P. Pandi, C. Gopinathan, Synthesis and characterization of TiO$_2$-NiO and TiO$_2$-WO$_3$ nanocomposites, J. Mater. Sci. Mater. Electron. 28 (2017) 5222–5234.

[55] J. Zhou, G. Tian, Y. Chen, J.-Q. Wang, X. Cao, Y. Shi, K. Pan, H. Fu, Synthesis of hierarchical TiO$_2$ nanoflower with anatase-rutile heterojunction as Ag support for efficient visible-light photocatalytic activity, Dalton Trans. 42 (2013) 11242–11251.

[56] D. Reyes-Coronado, G. Rodríguez-Gattorno, M.E. Espinosa-Pesqueira, C. Cab, R. de Cross, G. Oskam, Phase-pure TiO$_2$ nanoparticles: anatase, brookite, and rutile, Nanotechnology 19 (2008) 145605–145614.

[57] Y.P. Varshni, Temperature dependence of the energy gap in semiconductors, Physica 34 (1967) 149–154.

[58] N.D. Abazović, M.I. Čomor, M.D. Dramićanin, D.J. Jovanović, S.P. Ahrenkiel, J. M. Nedeljković, J. Baran, Photoluminescence of anatase and rutile TiO$_2$ particles, J. Chem. B 110 (2006) 25366–25370.

[59] N. Daude, C. Gout, C. Jouanin, Electronic band structure of titanium dioxide, Phys. Rev. B 15 (1977) 3229–3235.

[60] L. Kernazhitsky, V. Shymanovska, T. Gavrilko, V. Naumov, L. Fedorenko, V. Kshnyakin, J. Baran, Room temperature photoluminescence of anatase and rutile TiO$_2$ powders, J. Lumin. 146 (2014) 199–204.

[61] X. Sun, J. Wu, F. Tian, W. Zhang, Q. Li, Synergistic effect of surface defect and interface heterostructure on TiO$_2$/BiOIO$_3$ photocatalytic oxide gas-phase mercury, Mater. Res. Bull. 103 (2018) 247–258.

[62] J. Liqiang, Q. Yichun, W. Baiqi, L. Shudan, J. Baojiang, Y. Libin, F. Wei, F. Honggang, S. Jiazhong, Review of photoluminescence performance of nano-sized semiconductor materials and its relationships with photocatalytic activity, Sol. Energy Mater. Sol. Cells 90 (2006) 1773–1787.

[63] H. Nakajima, T. Mori, Photoluminescence of Pt-loaded TiO$_2$ powder, Phys. B 376–377 (2006) 820–822.

[64] J. Zhang, P. Zhou, J. Liu, J. Yu, New understanding of the difference of photocatalytic activity among anatase, rutile and brookite TiO$_2$, Phys. Chem. Chem. Phys. 16 (2014) 20382–20386.

[65] J.J.M. Vequizo, H. Matsunaga, T. Ishiku, S. Kamimura, T. Ohno, A. Yamakata, Trapping-induced enhancement of photocatalytic activity on brookite TiO$_2$ powders: comparison with anatase and rutile TiO$_2$ powders, ACS Catal. 7 (2017) 2644–2651.

[66] B. Song, G. Chao, L. Jingxiang, X. Yujie, Crystal phase engineering on photocatalytic materials for energy and environmental applications, Nano Res 12 (2019) 2031–2054.

[67] H. Sopha, M. Krbal, S. Ng, J. Prikryl, R. Zazpe, F.K. Yam, J.M. Macak, Scaling up anodic TiO$_2$ nanotube layers for gas phase photocatalysis, Appl. Mater. Today 9 (2017) 104–110.

[68] U. Chinonso, O. Ibukun, H.K. Jeong, Air plasma treated TiO$_2$/MWCNT composite for enhanced photocatalytic activity, Chem. Phys. Lett. 757 (2020), 137850.

[69] B. Moss, K.K. Lim, A. Beltram, S. Moniz, J. Tang, P. Fornasiero, P. Barnes, J. Durrant, A. Kafizas, Comparing photoelectrochemical water oxidation, recombination kinetics and charge trapping in the three polymorphs of TiO$_2$, Sci. Rep. 7 (2017) 2938.

[70] F.-X. Xiao, J. Miao, B. Liu, Layer-by-layer self-assembly of CdS quantum dots/graphene nanosheets hybrid films for photoelectrochemical and photocatalytic applications, J. Am. Chem. Soc. 136 (2014) 1559–1569.

[71] X.T. Wang, C.H. Liow, D.P. Qi, B.W. Zhu, W.R. Leow, H. Wang, C. Xue, X.D. Chen, S.Z. Li, Programmable photo-electrochemical hydrogen evolution based on multi-segmented CdS-Au nanorod arrays, Adv. Mater. 26 (2014) 3506–3512.

[72] V. Brezová, D. Dvoraková, A. Staško, Characterization of titanium dioxide photoactivity following the formation of radicals by EPR spectroscopy, Res. Chem. Intermed. 33 (2007) 251–268.

[73] H. Czili, A. Horváth, Applicability of coumarin for detecting and measuring hydroxyl radicals generated by photoexcitation of TiO$_2$ nanoparticles, Appl. Catal. B 81 (2008) 295–302.

[74] Z. Barbieriková, D. Dvoranová, M.-V. Sofianou, C. Trapalis, V. Brezová, UV-induced reactions of Mg^{2+}-doped anatase nanocrystals with exposed {0 0 1} facets: An EPR study, J. Catal. 331 (2015) 39–48.

[75] T. Kawahara, Y. Konishi, H. Tada, N. Tohge, J. Nishii, S. Ito, A patterned TiO_2(anatase)/TiO_2(rutile) bilayer-type photocatalyst: Effect of the anatase/rutile junction on the photocatalytic activity, Angew. Chem. Int. Ed. 41 (2002) 2811–2813.

[76] R. Ma, T. Chen, Checking the synergetic effect between anatase and rutile, J. Phys. Chem. C. 123 (2019) 19479–19485.

[77] S. Grant, A.A. Freer, J.M. Winfield, C. Gray, T.L. Overtonc, D. Lennon, An undergraduate teaching exercise that explores contemporary issues in the manufacture of titanium dioxide on the industrial scale, Green. Chem. 6 (2004) 25–32.

[78] S.N. Ahmed, W. Haider, Heterogeneous photocatalysis and its potential applications in water and wastewater treatment: a review, Nanotechnology 34 (2018), 342001.

[79] J. Wang, W. Sun, Z. Zhang, Z. Jiang, X. Wang, R. Xu, R. Li, X. Zhang, Preparation of Fe-doped mixed crystal TiO_2 catalyst and investigation of its sonocatalytic activity during degradation of azo fuchsine under ultrasonic irradiation, J. Colloid Interface Sci. 320 (2008) 202–209.

[80] S. Yang, W. Zhu, J. Wang, Z. Chen, Catalytic wet air oxidation of phenol over CeO_2-TiO_2 catalyst in the batch reactor and the packed-bed reactor, J. Hazard. Mater. 153 (2008) 1248–1253.